Nanowire Electromechanical Switch as a Tool for Surface Characterization

by

Sepeedeh Shahbeigi Roudposhti

A Dissertation Submitted to the
Graduate School of Sciences and Engineering
in Partial Fulfillment of the Requirements for
the Degree of

Master of Science

in

Mechanical Engineering

KOÇ UNIVERSITY

August 2, 2019

Nanowire Electromechanical Switch as a Tool for Surface Characterization

Koç University

Graduate School of Sciences and Engineering

This is to certify that I have examined this copy of a master's thesis by

Sepeedeh Shahbeigi Roudposhti

and have found that it is complete and satisfactory in all respects,
and that any and all revisions required by the final
examining committee have been made.

Committee Members:

Assoc. Prof. Dr. Erdem Alaca

Asst. Prof. Dr. Sedat Nizamoğlu

Prof. Dr. Arda D. Yalçınkaya

Date:

To my beloved parents

ABSTRACT

The benefits of downscaling electromechanical systems have been demonstrated in the form of NEMS with high performance and low power consumption. Silicon nanowires (Si NWs) are one of the leading devices with a remarkable potential in the field of sensing and actuation. While improvements in Q-factor and resonance frequency have been obtained through miniaturization enabling further capabilities, the change in their physical properties is a direct outcome of size reduction. In this aspect size dependence of the mechanical behavior is mainly attributed to the significant contribution of surface area. Various attempts have been carried out to study the scale effect on the mechanical behavior of Si NWs. However, existing Modelling methods still fail to reproduce experimental findings. Moreover, fabrication of Si NWs with extreme dimensions imposes a significant challenge to study the scale effect on the mechanical properties of Si NWs.

Utilizing the recently introduced field-emission scanning probe lithography (FE-SPL) in combination with cryogenic etching this study aims to generate Si NW switches. Secondary electrons emitted with Low energy are used in FE-SPL lithography, in contrast to previous methods, to minimize the proximity effects for high resolution patterning at ambient temperatures and room condition. The fabrication process is utilized to pattern a wide range of dimensions with lengths from 2 μm to 4 μm, widths from 40 nm to 100 nm and an average gap of 50 nm between each NW and electrodes. The fabrication process is developed on a silicon-on-insulator (SOI) substrate with a 14-nm-thick device layer.

These switches are then utilized for the purpose of surface characterization, as pull-in voltage -as a straightforward parameter to charactrize - depends heavily on surface elasticity and surface stress. Both comprite the leading properties of surfaces, which

are very challenging to quantify. For this purpose, a multiphysics modeling technique is developed based on finite element analysis. NW deflection is estimated based on the modified Young-Laplace equation. Pull-in voltage is calculated for fixed-fixed and fixed-free boundary conditions. Remarkable size and boundary condition effects are obtained for Si NWs with high aspect ratios. These effects have been analyzed and a model to describe them is suggested.

In the current project, we are aiming to address controversies observed in the surface contribution to the mechanical properties of Silicon through pull-in voltage measurements in silicon nanowire switches. Nanowires with high aspect ratios are being fabricated and a numerical model has been developed to model the electromechanical behavior of a silicon nanowire switch. Moreover, a methodology and measurement procedure is designed to extract the surface elasticity and surface stress parameters by utilizing the experimental and numerical results.

ÖZETÇE

Küçültülmüş boyutların elektromekanik sistemlere faydaları, yüksek performans ve düşük güç tüketimi ile NEMS şeklinde gösterilmiştir. Silikon nanoteller (SiNW) algılama ve aktivasyon alanında dikkat çekici potansiyele sahip önde gelen cihazlardan biridir. Daha fazla özellik için minyatürizasyon yoluyla Q-faktörü ve tınlaşım frekansını geliştirirken, fiziksel özelliklerindeki değişim, boyut azalımınım doğrudan bir sonucudur. Mekanik davranışa olan boyut bağımlılığı esas olarak yüzey alanının önemli katkısına atfedilir. SiNW'in mekanik davranışı üzerindeki ölçek etkisini incelemek için çeşitli girişimler yapılmıştır. Bununla birlikte, modelleme yöntemleri hala deneysel bulgulara tam olarak uymamaktadır. Ayrıca, SiNW'in yüksek boyutlara sahip imalatı, SiNW'in mekanik özellikleri üzerindeki ölçek etkisini incelemek için zorluklar getirmektedir. Termal oksitlenme küçülmek için şimdiye kadar kullanılmıştır. Bununla birlikte, yüzey oksitlenme oluşumu ve boyutu azaltmak için yüksek sıcaklık oksitlenme süreçleri tarafından uygulanan gerilmeler, mekanik davranışın belirlenmesi için zorluklar oluşturmaktadır. Son zamanlarda, nano-ölçekli cihazların imalatı için bir alan salınımlı tarama prob litografisi (FE-SPL) geliştirilmiştir. Bu çalışmada, SiNW anahtarları üretmek için FE-SPL ve kriyojenik aşındırma kombinasyonunu kullandık. Düşük enerjili yayılan ikincil elektronlar, ortam sıcaklıklarında ve oda koşullarında yüksek çözünürlüklü desenlendirme için yakınlık etkilerini en aza indirgemek için, önceki yöntemlerin aksine, FE-SPL litografisinde kullanılır. Üretim süreci, 2 μm'den 4 μm'ye kadar geniş bir boyut yelpazesini, 40 nm'den 100 nm'ye kadar genişliği ve NW ve elektrotlar arasında ortalama 50 Nm'lik bir boşluğu modellemek için kullanılır. Üretim süreci, 14 nm kalınlığında cihaz tabakasına sahip bir silikon-üzeri-izolatör (SOI) substrat üzerinde geliştirilmiştir. FE-SPL'NİN yakın döngü litografi tekniği, çalışma alanının ön görüntülemesini, litografi sürecini

ve rölenin kendi kendini harekete geçiren ve kendi kendini algılayan konsol uçlarını kullanarak post-görüntülemesini sağlar. SiNW'in operasyonel davranışı üzerindeki yüzey etkisini incelemek için sonlu elemanlar analizine (FEA) dayalı çok fizikli bir modelleme tekniği geliştirilmiştir. NW algılama modifiyeli Young-Laplace denklemine göre tahmin edilmektedir. Çekme-gerilimi sabit-sabit serbest sınır koşulları için hesaplanır. SiNW'nin çekme-gerilimi üzerinde yüksek en boy oranlarına sahip dikkate değer bir boyut ve sınır durumu etkisi elde edilir. Bu etkiler nicel ve niteliksel olarak analiz edilmiş ve bunları tanımlamak için bir model önerilmiştir. Bu çalışma, deneysel bulgular ve önerilen model arasında bir karşılaştırma yapacaktır. Deney sonuçları SiNW yüzey karakterizasyonu için kullanılacaktır. Bu yaklaşım, yüzey etkisinin SiNW mekanik davranışı üzerindeki çalışmasında tınlaşım ve gerginlik testi gibi alternatiflere kıyasla oldukça basit bir teknikte çekme-kullanımını kolaylaştırır.

ACKNOWLEDGMENTS

I would like to express my great appreciation to Prof. Dr. Alaca for his patient guidance, enthusiastic encouragement and useful critiques of this research work. His willingness to give his time so generously has been very much appreciated. I would also like to thank Dr. Nasr Esfahani for his advice and assistance during the course of this project. I would also like to acknowledge Prof. Dr. Ivo Rangelow and Mr. Hoffman at the technical university of Ilmenau for their help and constructive recommendation on the fabrication processes. My grateful thanks are also extended to Mr. Yazgi Guneri and Mr. Bicer for their help in offering me resources in the cleanroom.

Finally, I wish to thank my parents for their support and encouragement throughout my study.

TABLE OF CONTENTS

LIST OF TABLES

LIST OF FIGURES

NOMENCLATURE

NW	Nanowire
NEMS	Nanoelectromechanical systems
L	Lenght
b	Width
t	Thickness
F_{elec}	Electromechanical force
V_{pi}	Pull-in voltage
FEA	Finite element analysis
$w(x)$	Transverse displacement
x	Longitudinal coordinate
P^{*}	Uniaxial force
IC	Integrated circuit
ϵ_0	Dielectric permittivity
V	Bias voltage
g_0	Initial gap
$(EI)_{eff}$	Effective bending rigidity
I	Second moment of inertia
E_0	Bulk Young's modulus
$\hat{\sigma}$	Stress
$\hat{\tau}$	Surface stress
I_s	Surface second moment of inertia
τ_0	Initial surface stress
k	Mechanical stiffness

Chapter 1

INTRODUCTION

Extensive economic motivations have forced the semiconductor manufacturing industry to follow the Moore's law. Increasing the density of the transistors per area of a chip has proved to be very advantageous in the sense of power consumption and capability. Nanowires as the basic building block for nanoelectromechanical system (NEMS) devices also follow the same trend. However, this size reduction introduces challenges in the electromechanical behavior of the features. Now that the surface area to volume ratio of the NW has increased, the previously intrinsic properties of the material change due to the surface effect. Experimental and theoretical studies have been carried out throughout the past decade to understand the surface contribution to the mechanical behavior of the NWs. These studies mainly yield contradictory outcomes and demonstrate the difficulty in predicting silicon NWs behavior. This thesis intends to address these controversies and close the gap between the theoretical and experimental works. For this matter, the project consists of two parts: 1- a numerical model to calculate the electromechanical parameters of the NWs. 2- an experimental part which includes the fabrication of the silicon NWs.

In chapter 2, the NW is assumed to consist of a bulk and very thin surface parts. Then utilizing the composite beam theory, an effective mechanical property is assigned to the NW. The electromechanical parameters are calculated using the modified Young-Laplace equation for various geometries and boundary conditions. Furthermore, a sensitivity analysis is carried out on the dimensions and boundary conditions.

Fabricating structures with extreme nanoscale dimensions is another obstacle in studying the surface contribution to the mechanical behavior of the NWs. A field-emission scanning probe lithography technique is introduced in the third chapter that has overcome some difficulties in the fabrication of features in the nano regime. The lithography is followed by a cryogenic ion etching process to transfer the pattern to the silicon.

In chapter 4, an experimental setup and a method to extract the surface parameters are proposed. The method will merge the outcome of the previous two chapters.

Chapter 2

SURFACE EFFECT ON THE OPERATION OF THE NANOWIRE SWITCHES

2.1 Overview

Nanowires (NWs) are fundamental building block in nanoelectromechanical systems (NEMS) for sensing and actuation purposes (Ma et al., 2010; Bargatin et al., 2012; Ekinci and Roukes, 2006; Yang et al., 2006; Kozinsky et al., 2006a; Esfahani et al., 2018a; Ionescu and Riel, 2011). There are various functionality for NEMS devices including resonance (Feng et al., 2007; He et al., 2008) and quasi-static in a switch form (Han et al., 2010; Li et al., 2007). Understanding their operational behavior is the preliminary step in designing and implementation. A simple nanowire switch is basically a beam-like structure and an electrostatic nearby electrode as depicted in figure 2.1. The electrostatic force between nanowire and electrode constitutes a bending deflection. If voltage is increased beyond a critical value, the beam will abruptly touch the electrode. This voltage is called "pull-in voltage", V_{pi}, which is a crucial design parameter in nanowire switches.

In extreme dimensions, the surface area of the nanobeam is considerable compared to its volume. Therefore, the surface effect must be considered in the overall properties of the structure. In this chapter, to investigate surface effects, generalized Young-Laplace equation is used to model an electrostatically actuated beam deflection via finite element analysis (FEA). The applied bias voltage is increased to reach V_{pi}. Furthermore, a sensitivity analysis is conducted with respect to the dimension parameters. The incorporation of the surface effect and electric softening is studied for two different boundary conditions: fixed-fixed and fixed-free (cantilever) boundary conditions. Results demonstrate the importance of surface effects in selecting the design parameters in NEMS switches such as pull-in voltage. The length-to-thickness ratio is found to be a suitable parameter to express the surface effect rather than the surface-area-to-volume ratio. The model in this chapter will be used to extract the surface properties of the NWs by measuring their pull-in voltage experimentally (chapter 3).

2.2 Introduction

NEMS devices have been studied theoretically and experimentally for decades through introducing various applications in sensing and actuation (Ma et al., 2010; Ekinci and Roukes, 2006; Bargatin et al., 2012; Yang et al., 2006). The potential for mass sensing about zepto-gram (Feng et al., 2007) and frequency more than gigahertz (Ekinci and Roukes, 2006) has been demonstrated through using NEMS. With the benefits of size reduction, such as higher sensitivity, lower mass, and higher Q factors, now researchers are focusing on Nano-scale devices to embark on new application possibilities. In this scope, NWs have drawn attention due to their unique properties (Ma et al., 2010) and compatibility with integrated circuits (ICs) (Arkan et al., 2011). However, miniaturization of NWs offers further capabilities on sensing and actuation applications, size effects contributes on the mechanical properties through significant surface effects (Wang and Wang, 2014; Esfahani and Alaca, 2019). This size dependency plays an important role in defining the design parameters of NWs.

NW switches are generally beam-like structures undergoing electrostatic force and following bending deformation(Kozinsky et al., 2006b; Arkan et al., 2011; Esfahani et al., 2018b). A simple switch has two ports of a suspended nanowire and a fixed electrode as shown in figure 2.1. Deformation is achieved through applying electrostatic force induced as a voltage difference between NW and electrode. Increasing the voltage imposes more deflection to a certain level, where the NW touches the electrode. This phenomena is called pull-in instability. So far, theoretical and experimental studies have displayed a contrasting outcome regarding the size dependency of electromechanical characteristics of the NW switches. The difference in the outcomes is known to be due to the different properties of the atoms laying on the surface of the NW with that of the bulk. Moreover, the size reduction to sub-micron regime makes a significant contribution of the surface to the overall properties. As an instance of important property to model the behavior of NW switches with significant surface-to-volume ratio, the bulk Young's modulus will be replaced with effective Young's modulus (He et al., 2008).

To study the size-dependent elastic modulus, He et al. (2008) propose a closed-form analytical solution to calculate the effective bending rigidity based on Young-Laplace equation. Song et al. (2011) improved the aforementioned model by accounting the initial stresses, which their result is then validated by experimental results (Babaei Gavan et al., 2009) to estimate the effective Young's modulus for silicon nitride cantilevers. In another study, Miller and Shenoy (2000) have proposed a simple model to relate a non-dimensional bending rigidity parameter to the size of the structural element, surface parameter and bulk properties, where their results are in agreement with atomic force simulations. However, deficiencies associated with this model is difficulties on utilizing materials with arbitrary atomic structures. Hu et al. (2004) have investigated the electromechanical behavior of a microcantilever-type switch and proposed a modal expansion method to analytically solve for the deflection of the beam. Later in the article, they verify their analytical model by the results from an experiment. Moreover, Nasr and Alaca (2018) have studied the effect of crystal orientation on electromechanical behavior of NWs as a contributing factor to pull-in as well. Sadeghian et al. (2009) have measured the pull-in voltage of nanocantilevers with various dimensions and based on experimental observations have proposed a rough model to estimate the effective Young's modulus of the structure. Furthermore, Li et al. (2003b) have measured the size effect on the mechanical properties of silicon nanocantilevers by resonance method. Fu and Zhang (2011) have presented a modified continuum model for electrostatically actuated nanobeams using the surface elasticity. Ma et al. (2010) and Wang and Wang (2014) have both included the effect

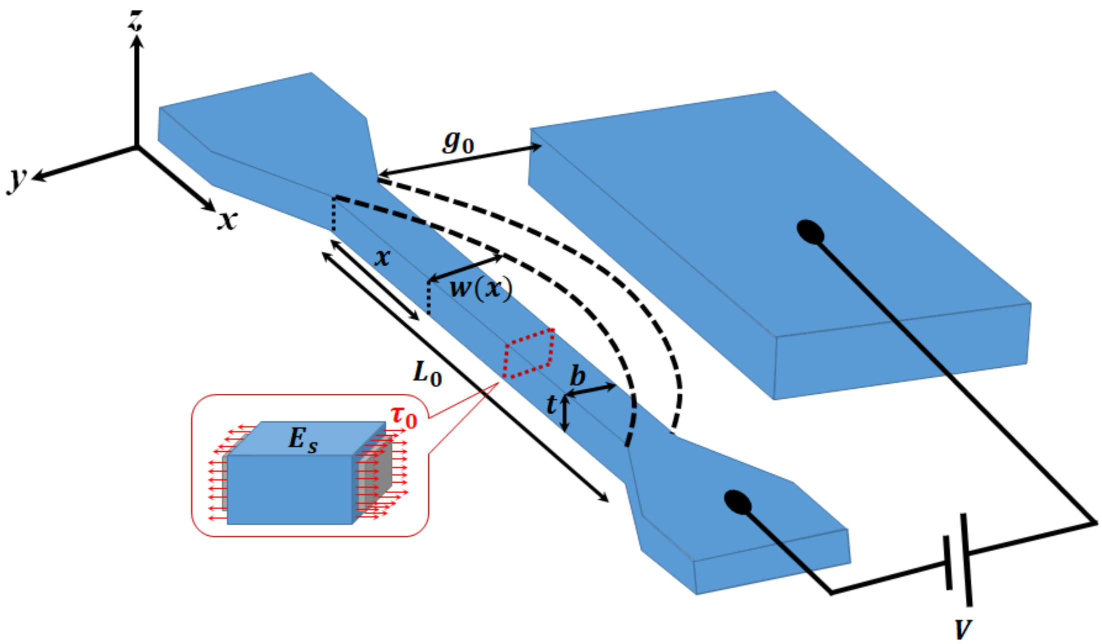

Figure 2.1: NW with a nearby electrode. The inset indicate the NW cross-section with surface effects including surface stress, τ, and surface elasticity, E_s.

of Casimir force on the electromechanical behavior of the nanocantilevers.

Although many studies have been carried out on the influence of surface effect, none of them are studying the incorporation of electric softening due to bending and the surface effect by considering the effective parameters involved such as geometrical parameters and boundary conditions. Numerical models are advantageous since they are efficient and simple, however still work is needed to close the gap between theoretical and experimental works. The numerical model developed in this chapter, will be used to estimate the surface properties of the fabricated NWs of the experimental part of this research. The modified Young-Laplace model of this chapter is numerically solved to calculate the deflection and pull-in voltage of fixed-fixed and fixed-free nanobeams including the surface effects and electric softening. The importance of various physics including electric softening and the surface effect on the operational behavior of NW switches is studied as a function of geometrical parameters and boundary conditions. In the rest of the chapter first, the physics is described, then the numerical model is explained. The numerical results and conclusions will be presented afterwards.

2.3 Governing Equation

The equation governing the static bending of a NW with length, L, width, b, and thickness, t, as illustrated in figure 2.1, undergoing an electrostatic force along its length is developed from the Euler-Bernoulli beam theory as:

$$(EI)_{eff}\frac{d^4w(x)}{dx^4} - P^*\frac{d^2w(x)}{dx^2} = F_{elec}(x) \tag{2.1}$$

where, $w(x)$ is the transverse displacement of the NW, x is the longitudinal direction. P^* is the uniaxial loading term including residual stress and surface stress. F_{elec} is the electrostatic force exerted along the NW as:

$$F_{elec}(x) = \frac{1}{2}\frac{\epsilon_0 V^2 b}{(g_0 - w(x))^2} \tag{2.2}$$

where $\epsilon_0 = 8.85 \times 10^{-12}\ C^2N^{-1}m^{-2}$ is the dielectric permittivity of air. V is the applied voltage between two electrodes. g_0 is the initial gap. $(EI)_{eff}$ is the effective bending rigidity of the NW. E is the Young's modulus and I is the second moment of inertia. In equation 2.2, the distributed electrostatic force is a nonlinear function of the gap between NW and electrode, where the bending deformation causes an increase on the electrostatic force. Therefore, the reduction of electrostatic gap applies further bending in NW, which is called electric softening. Including the geometrical nonlinearities in the Young-Laplace model, the atoms laying on the surface of the beam will experience a different stress than the bulk of the structure and an axial stress will be formed along the surface of the beam (Song et al., 2011). Therefore, when surface area to volume ratio is passed a certain point, the structures mechanical properties will be different from the materials bulk properties.

Based on Young-Laplace model, the in-plane stresses in curved surfaces are a cause for out-of-plane stresses (Song et al., 2011). The common approach here is to assume that the beam is consisted of a bulk body and a very thin surface (figure 2.1). Then the effective young's modulus is calculated by the composite beam theory. He et al.

(2008) have proposed an analytical solution for E_{eff} as follows

$$(\frac{E_{eff}}{E_0})_{fixed/fixed} = \frac{P^* L^2}{4E_0 bt^3[1 - \frac{4tanh(\sqrt{\eta}/4)}{\sqrt{\eta}}]} \tag{2.3}$$

$$(\frac{E_{eff}}{E_0})_{fixed/free} = \frac{4P^* L^2}{E_0 bt^3 cosh(\sqrt{\eta})[1 - \frac{tanh(\sqrt{\eta})}{\sqrt{\eta}}]} \tag{2.4}$$

Table 2.1: Comparison of He et al. (2008) and Song et al. (2011) models

Model	P^*	$(EI)^*$
Song et al. (2011)	$bt\tilde{\sigma} + 2(b+t)\tilde{\tau}$	$E_0 I + \tilde{\sigma} I + (E_s + \tilde{\tau}) I_s$
He et al. (2008)	$bt\tilde{\sigma} + 2b\tilde{\tau}$	$E_0 I + \tilde{\sigma} I + E_s I_s$

In these equations E_0 is the bulk Young's modulus. $\eta = P^* L^2/(EI)^*$ is the nondimensional surface effect factor. Assuming that the initial stresses and strains are constant in each cross section (Song et al., 2011), for a rectangular cross section beam (figure 2.1), the effective bending modulus is expressed as:

$$(EI)^* = E_0 I + \tilde{\sigma} I + (E_s + \tilde{\tau}) I_s \tag{2.5}$$

where $I = \frac{bh^3}{12}$ and $I_s = \frac{bh^2}{2} + \frac{h^3}{6}$ in which surface layer thickness is infinitesimally small compared to bulk dimensions. E_s is the thin surface's young modulus. Axial initial stress $\tilde{\sigma}$, and total initial surface stress $\tilde{\tau}$, are respectively given by:

$$\tilde{\sigma} = E_0 \tilde{\epsilon} \tag{2.6}$$

$$\tilde{\tau} = \tau_0 + E_s \tilde{\epsilon}^s \tag{2.7}$$

τ_0 denotes the strain independent part of the total surface initial stress. If $\hat{\tau}$ is ignored, the model will be that of He et al. (2008). As mentioned before, the in-plane surface stresses will cause also a transverse loading P^* on the NW along it's curvature

Table 2.2: Governing equations for cases considering different physics

Case no.	Physical properties considered	Governing Equation
1	Electric softening and surface stress	$(EI)_{eff}\frac{d^4w}{dx^4} - P^*\frac{d^2w(x)}{dx^2} = \frac{\epsilon_0 bV^2}{2(g-w(x))^2}$
2	Electric softening	$E_0I\frac{d^4w}{dx^4} = \frac{\epsilon_0 bV^2}{2(g-w(x))^2}$
3	Surface stress	$(EI)_{eff}\frac{d^4w}{dx^4} - P^*\frac{d^2w(x)}{dx^2} = \frac{\epsilon_0 bV^2}{2g^2}$
4	Simple	$E_0I\frac{d^4w}{dx^4} = \frac{\epsilon_0 bV^2}{2g^2}$

$(\frac{d^2w(x)}{dx^2})$, modeled in eq. 2.1. The beam may react as stiffer or softer when it is loaded, depending on its boundary conditions. The loading is expressed in equation 2.8:

$$P^* = bt\tilde{\sigma} + 2(b+t)\tilde{\tau} \tag{2.8}$$

if thickness is not included in equation 2.8, the He et al. (2008) expression for the force will be acquired. For clarification, the differences for two models are mentioned in table 2.1.

In this chapter, equation 2.1 is solved for four different cases based on corresponding physics involved into the model. Cases are summarized in the Table 2.2. Case 1 is the case including the effects of surface and electric softening, whereas, in case 2 surface effects is ignored and in case 3 electric softening is not included. Case 4 is the simplest case, in which both electric softening and surface stress are ignored.

2.3.1 Analytical Solution for Deflection

Many closed-form analytical solutions have been proposed for equation 2.1. For instance, Hu et al. (2004) use second order Taylor expansion to linearize the nonlinear electrical pressure term; Therefore, equation 2.1 will be rewritten as follows:

$$(EI)^{*}\frac{d^4w(x)}{dx^4} - P^{*}\frac{d^2w(x)}{dx^2} - \frac{\epsilon_0 bV^2}{g_0^3}w = \frac{\epsilon_0 bV^2}{2g_0^2} \tag{2.9}$$

Then the linear ordinary differential equation is discretized using the modal expansion method, where the deflection is described as

$$w(x) = \sum_{j=1}^{n} \beta_j \phi_j(x), \qquad n \to \infty \tag{2.10}$$

Where $\phi_j(x)$ is the jth natural mode of the structure and β_j is the associated modal participation factor. The natural modes of cantilever beam are

$$\phi_j(x) = (cosh\lambda_j x - cos\lambda_j x) - \sigma_j(sinh\lambda_j x - sin\lambda_j x), \tag{2.11}$$

$$\sigma_j = \frac{sinh\lambda_j L - sin\lambda_j L}{cosh\lambda_j L + cos\lambda_j L}, \tag{2.12}$$

and λ_j satisfies

$$1 + cos(\lambda_j L)cosh(\lambda_j L) = 0 \tag{2.13}$$

By replacing equation 2.10 in equation 2.9 and integrating along the length, the following modal participation factor and deflection for a electrostatically actuated cantilever are achieved

$$\eta_j = \frac{F_j}{k_j^m - k_j^e}, \tag{2.14}$$

$$w(x) = \sum_{j=1}^{n} \frac{F_j \phi_j(x)}{k_j^m - k_j^e} \tag{2.15}$$

where F_j is a general force term and

$$k_j^m = EI\lambda_j^4 \int_0^L \phi_j^2 dx = EI\lambda_j^4 L, \tag{2.16}$$

$$k_j^e = \frac{\epsilon_0 bV^2}{G^3} \int_0^L \phi_j^2 dx = \frac{\epsilon_0 bV^2 L}{g_0^3} \tag{2.17}$$

One can solve equation 2.1 through considering a constant gap and electrostatic force with neglecting the surface effect (similar to case 4) to estimate V_{pi} as Ou and Chen (2014)

$$V_{pi} = \sqrt{\frac{8kg_0^3}{27\epsilon_0 A}} \tag{2.18}$$

where k is the mechanical stiffness of the NW and A is the electrode area ($A = L \times t$ in figure 2.1).

2.4 Numerical Modeling

Equation 2.1 is nonlinear in nature, while analytical solutions have been proposed to approximate its solution (Hu et al., 2004; Goosen et al., 2009; Zhang et al., 2013; He et al., 2008). However, the analytical solutions are only limited to narrow range of problems with neglecting electric softening. On the other hand, numerical techniques are comparably more flexible.

In the present study, the Finite Element Analysis (FEA) has been used to model the deflection of the beam in electrostatically actuated beam with two different boundary conditions: 1- fixed-free beam (cantilever) 2- fixed-fixed beam.

According to FEA, if a beam is assumed as a 2D one-element-structure lying on the x-direction (figure 2.1), then each node of this element has two degrees of freedom (d.o.f), one in the transverse y-direction and the other rotational, $\theta = \frac{dw(x)}{x}$. Forces and moments generated due to differential movements in the direction of the d.o.f are perceived as positive and otherwise taken as negative. This model which only takes bending deformation into account is called elementary beam theory or Euler-Bernoulli beam theory.

The local stiffness matrix for each element for deformation in xy plane is:

$$[k] = \begin{bmatrix} \frac{12EI}{L^3} & \frac{6EI}{L^2} & -\frac{12EI}{L^3} & \frac{6EI}{L^2} \\ \frac{6EI}{L^2} & \frac{4EI}{L} & -\frac{6EI}{L^2} & \frac{2EI}{L} \\ -\frac{12EI}{L^3} & -\frac{6EI}{L^2} & \frac{12EI}{L^3} & -\frac{6EI}{L^2} \\ \frac{6EI}{L^2} & \frac{2EI}{L} & -\frac{6EI}{L^2} & \frac{4EI}{L} \end{bmatrix} \tag{2.19}$$

$[k]$ operates on the column vector of element d.o.f $[d] = [v_1, \quad \theta_1, \quad v_2, \quad \theta_2]^T$ in which subscripts 1 and 2 denote the starting and ending nodes respectively. If the order of the d.o.f is changed, the element stiffness matrix will change accordingly.

Then all elements stiffness matrices are combined consistently with considering the boundary conditions to form a global stiffness matrix $[k]_{global}$. The following constraints for fixed-free and fixed-fixed cases are applied to the global stiffness matrix:

1- The cantilever boundary condition:

v_1=0 degrees of freedom at first node

θ_1=0

2- The fixed-fixed boundary condition:

v_1=0 V_n=0 degrees of freedom at first and last nodes

θ_1=0 θ_n=0

After constructing the appropriate global stiffness matrix, the structures equilibrium equation is solved by the newton-Raphson method until the convergence is achieved.

2.5 Results and Discussion

In this section, first the numerical scheme will be verified through experimental studies. Following to verification, a comparison between He et al. (2008) and Song et al. (2011) will be carried out to study the differences concerning the initial surface stress. Then, results of a series of benchmark simulation will be presented to study the effect of geometrical parameters and boundary conditions on the surface contribution on pull-in voltage. The geometries considered to study the surface effect are listed in the table 2.3.

2.5.1 Model Verification

We proceed in this section by verifying the numerical model developed to calculate the V_{pi}. As a first step the convergence is tested by increasing the number of the elements. The bending deflection is calculated for different number of elements for a NW with length of 20 mm, width of 5 mm and thickness of 57 μm under an applied voltage of 40 V with an electrostatic gap of 92 μm. Figure 2.2 shows a convergence for number of elements more than 100. Now that the convergence is assured, a test case is chosen to verify the code. A cantilever with the parameters as defined in the

Table 2.3: Summary of geometries considered for NWs with various aspect ratios (AR) as the ratio of length-to-thickness (L/t) ($L\times b\times t$ all dimensions are in nm)

AR=8	AR=16	AR=24	AR=32
96×12×12	192×12×12	288×12×12	384×12×12
120×15×15	240×15×15	360×15×15	480×15×15
144×18×18	288×18×18	432×18×18	576×18×18
168×21×21	336×21×21	504×21×21	672×21×21
192×24×24	384×24×24	576×24×24	768×24×24
240×30×30	480×30×30	720×30×30	960×30×30

table 4.1 is modeled and the results are compared with experimental and analytical study on micro-beam pull-in (Hu et al., 2004). Figure 2.3 demonstrates an agreement between experimental measurements and the numerical model developed in section 1.4. The bending deformation of the cantilever is calculated through the proposed model. The surface effects has been ignored in this part.

2.5.2 Effective Young's modulus comparison for He et al. (2008) and Song et al. (2011) models

Many analytical models for the size dependency of the NW mechanical properties have been proposed so far. Here, the works of He et al. (2008) and Song et al. (2011) will be compared to also investigate the effect of considering initial surface stress. These models are based on modified Young-Laplace equation with a bulk/shell composition. Song et al. (2011) is a more recent model and covers some of the assumptions made in the model proposed by He et al. (2008). He et al. (2008) considers no initial stress

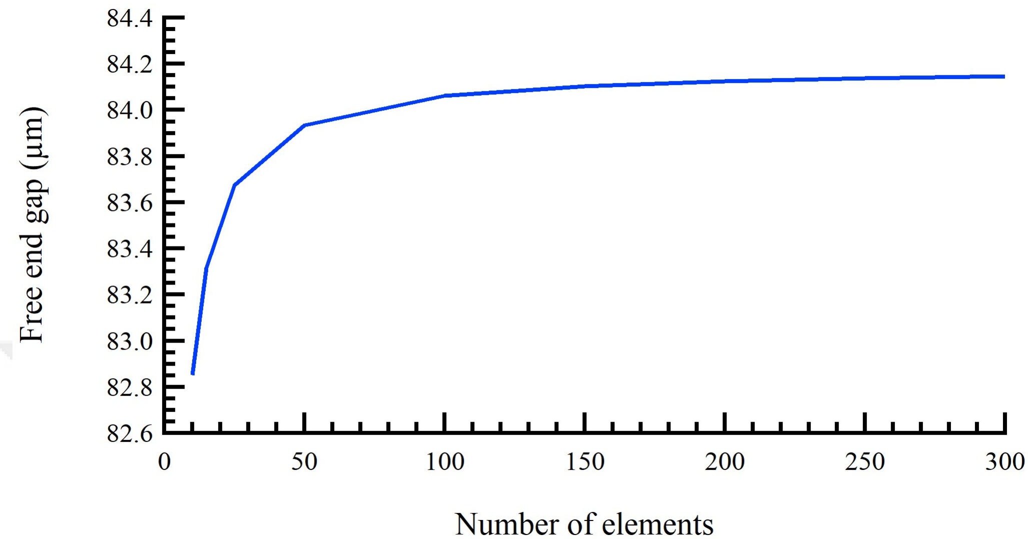

Figure 2.2: Free end gap vs. Number of elements for a NW with length of 20 mm, width of 5 mm, and thickness of 57 μm under applied voltage of 40 V and initial gap of 92 μm.

for the beam and ignore the effect of transverse surfaces on the elastic properties, whereas Song et al. (2011) take those parameters into account. The ratio of the effective Young's modulus to the bulk elastic modulus is calculated through equations 2.3 and 2.4 for different boundary conditions. The values considered for τ_0 and E_s are -0.88 N/m and -8.07 N/m respectively for $< 100 >$ silicon NWs (Yun and Park, 2012).

Results for geometrical parameters listed in table 2.3 are shown figure 2.4. Results show a dramatic boundary condition dependence of the effect of surface stress on E_{eff}. Furthermore, by increasing the aspect ratio, the initial surface stresses cause the effective Young's modulus and bulk modulus to deviate more. Results show a decrease in the effective Young's modulus with increasing NW length. This size dependency is more for lower widths. On the other hand, by increasing the cantilevers length, E_{eff} increases for cantilever boundary condition as in figure 2.4. In both boundary conditions, He et al. (2008) model appears to underestimate the effective Young's modulus which is also shown in Yun and Park (2012). This observation is reasonable

Table 2.4: Corresponding parameters for verification considered from experimental measurements (Hu et al., 2004)

Parameters	Values
Young's modulus (E) ($\frac{kg}{m^2}$)	155.8×10^9
Length (L) (mm)	20
Width (b) (mm)	5
Thickness (t) (μm)	57
Initial gap (g_0) (μm)	92

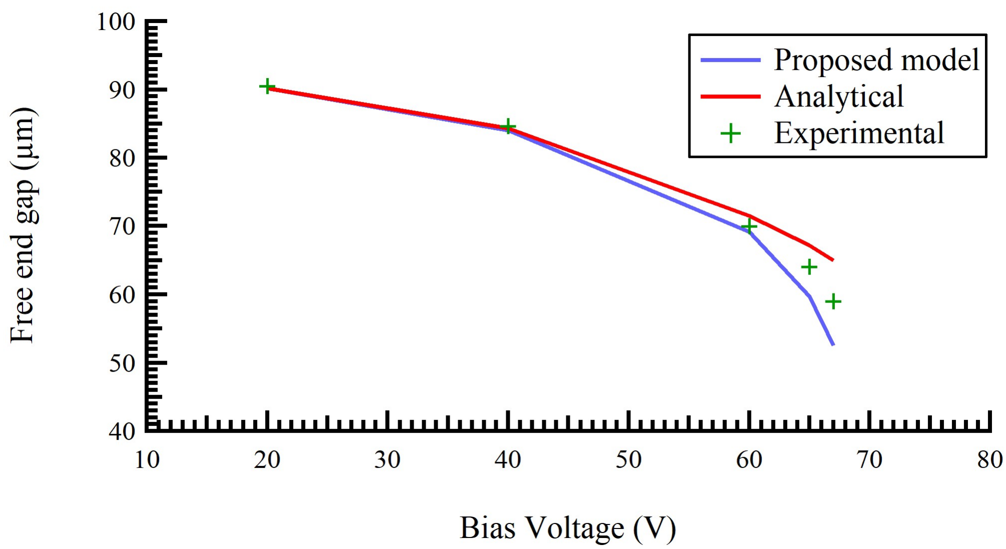

Figure 2.3: Tip displacement Vs. biased Voltage for the proposed model, Analytical (Hu et al., 2004) and experimental (Hu et al., 2004) comparisons

since they do not consider the intial surface stress and effect of two sides of the geometry into account. The rest of the thesis will use the Song et al. (2011) model to include the initial surface stress.

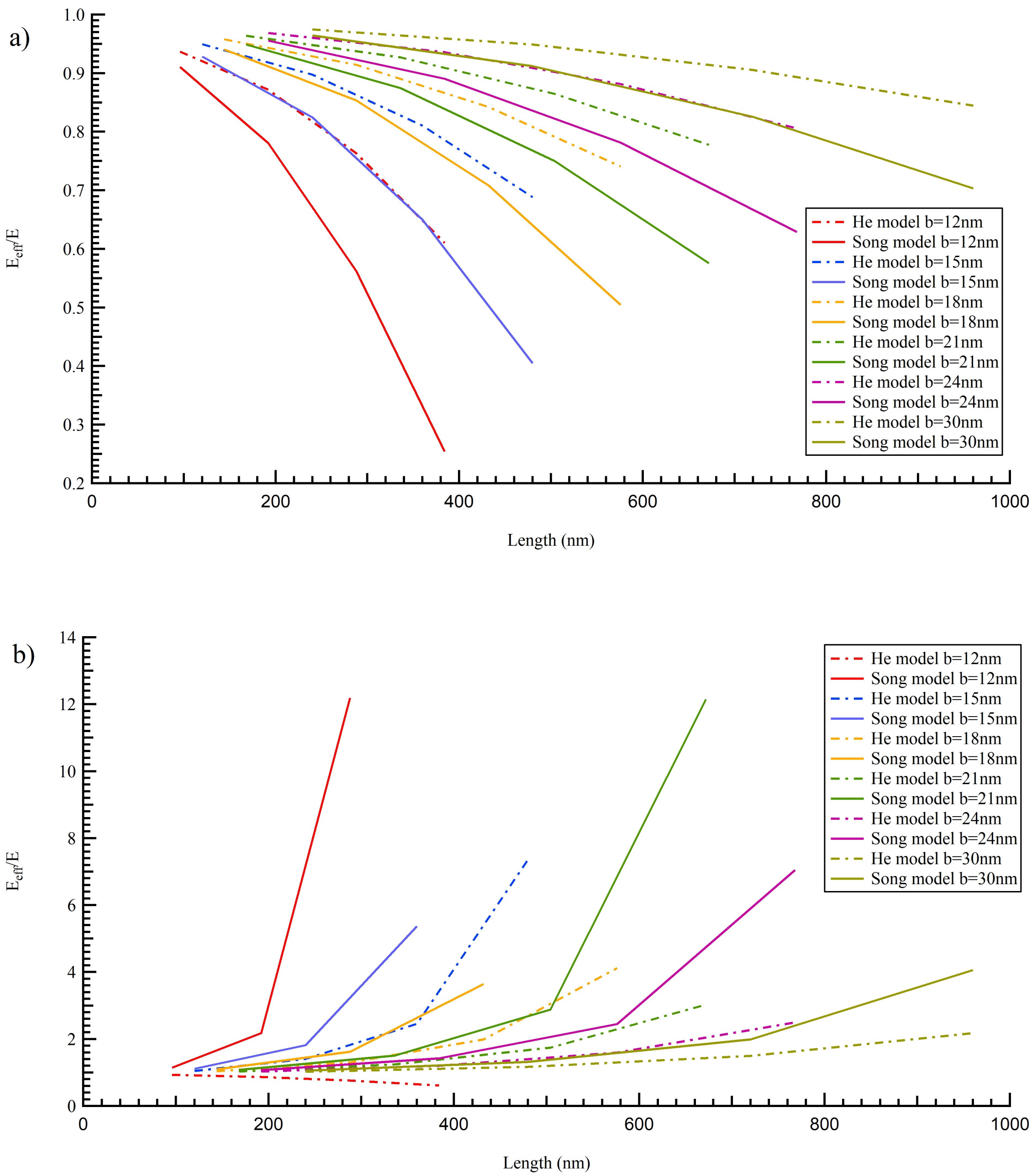

Figure 2.4: E_{eff}/E vs. Length for various NW dimensions in table 2.3 for: a) fixed-fixed b) cantilever boundary conditions

2.5.3 Results

We have considered four aspect ratios (AR) of 8, 16, 24, and 32. The initial gap is taken as 90 nm. The studied geometries are presented in table 2.3. The pull-in voltage, V_{pi}, is calculated through using the proposed FEM model. The pull-in voltage in all cases of 2, 3 and 4 - listed in the table 2.2 - are normalized with case 1 as the most accurate model for NW switches, $\bar{V}_{pi}$.

Figure 2.5 depicts the change in non-dimensional normalized pull-in voltage, $\bar{V}_{pi}$, for the fixed-fixed and cantilever boundary conditions with AR=24. The pull-in voltage values has been normalized with respect to the case where both electric softening and surface effects are taken into account. According to the figure 2.5.a, as the length increases the effect of surface reduced, which can be linked to decrease in the the SAV ratio with increasing L, while keeping the AR constant. Moreover, by comparing the simple case with the one which only surface effect is considered, it is concluded that surface effects will reduce the V_{pi} to values closer to the case where both surface effect and electric softening is accounted for. Another interesting point in figure 2.5 is that when considering only the surface effect into account the normalized pull-in voltage remains constant. In whichever of these cases, the electric softening effect is the more elemental factor.

Unlike the fixed-fixed, in cantilever boundary condition the surface effect changes the V_{pi} more by increasing the length in a constant aspect ratio as depicted in figure 2.5.b. However, again in the case where only the surface stresses are accounted for, $\bar{V}_{pi}$ does not change with length, though in cantilever the surface stress causes the pull-in voltage to deviate more from its actual value in case 3 comparing to the simple case.

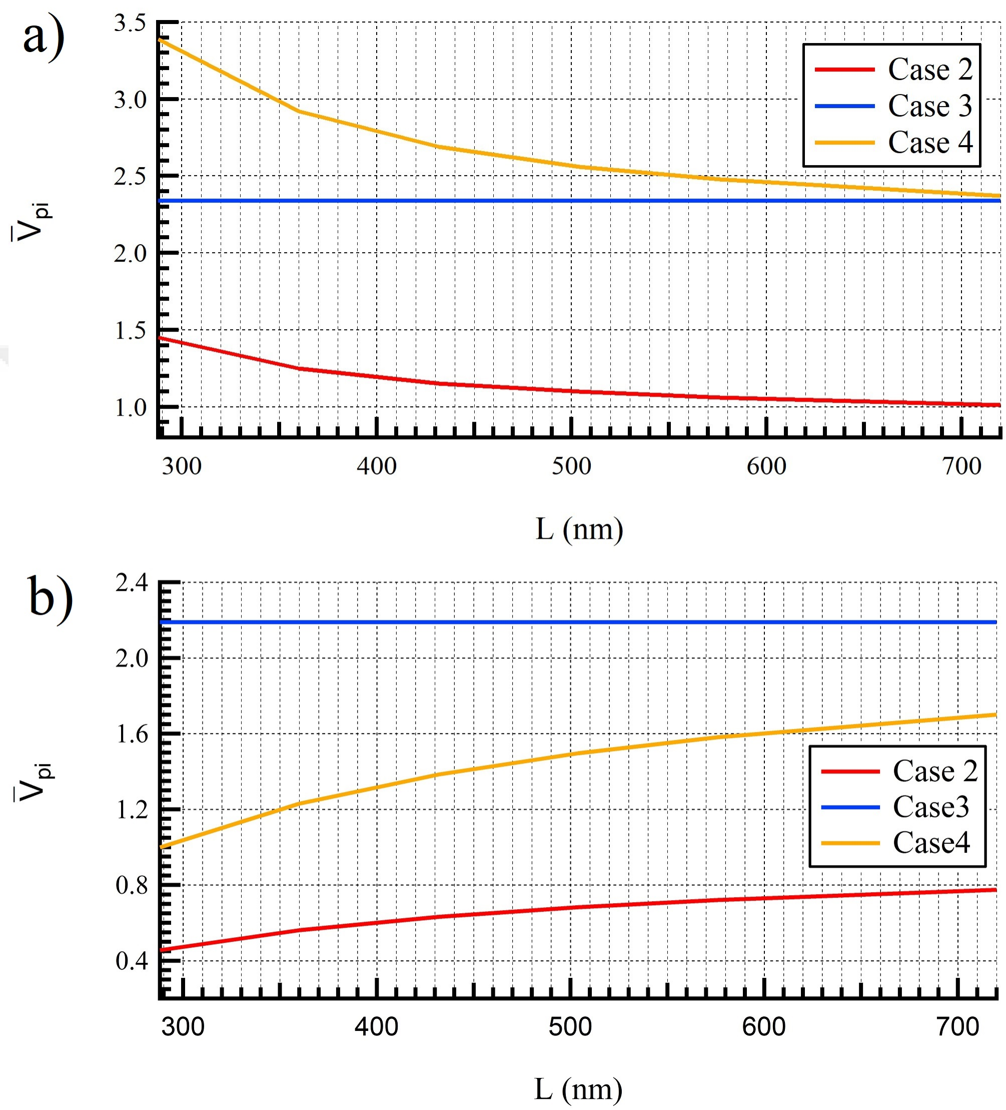

Figure 2.5: $\bar{V}_{pi}$ vs. L comparing the cases in table2.2 for AR=24 for: a) fixed-fixed b) Cantilever boundary conditions

The effect of thickness on calculated pull-in voltage for various aspect ratios in a fixed-fixed beam is illustrated in figure 2.6. So as the figure shows, decreasing the thickness will cause the surface effects to diminish. furthermore, in small aspect ratios, the surface effects has minimum contribution to the the V_{pi}. Therefore, it is concluded that the aspect ratio plays a more important role in pull-in voltage measurements compared to the other geometrical parameters. The importance of length-to-thickness ratio to include the surface effect on the mechanical response of NWs is demonstrated previously by studying the resonance properties (Yun and Park, 2012).

The effect of thickness on the surface contributions to the pull-in voltage in cantilevers is illustrated in figure 2.6.b. When aspect ratio is 8, all the calculated V_{pi} converge to a value close to the case 1 with including surface effect and electric softening, Therefore; surface contribution is minimum, regardless of the thickness. However, as the aspect ratio is increased towards 32, it can be seen that smaller thickness values demonstrate more surface contributions. As previously shown in figure 2.5.a, increasing length in a constant aspect ratio in fixed-fixed beams, diminishes the surface effects contribution to the pull-in voltage. In figure 2.7.a, it is also concluded that the decrease in aspect ratio, also decreases the geometrical sensitivity to the surface effect. Therefore, the aspect ratio is a defining parameter in the surface effects contribution to the pull-in voltage calculations.

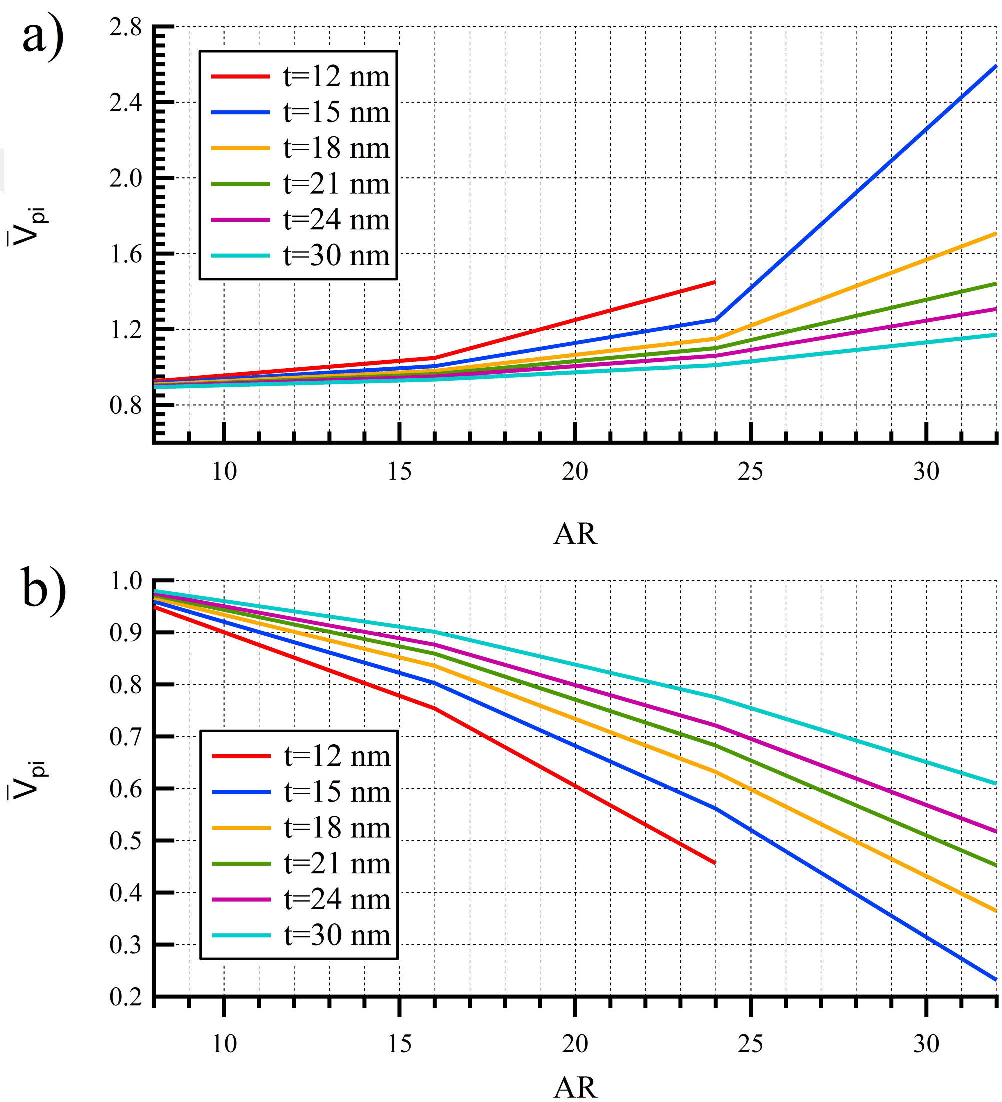

[H]

Figure 2.6: $\bar{V}_{pi}$ vs. AR for various thickness for case 2 in: a) fixed-fixed b) cantilever boundary conditions

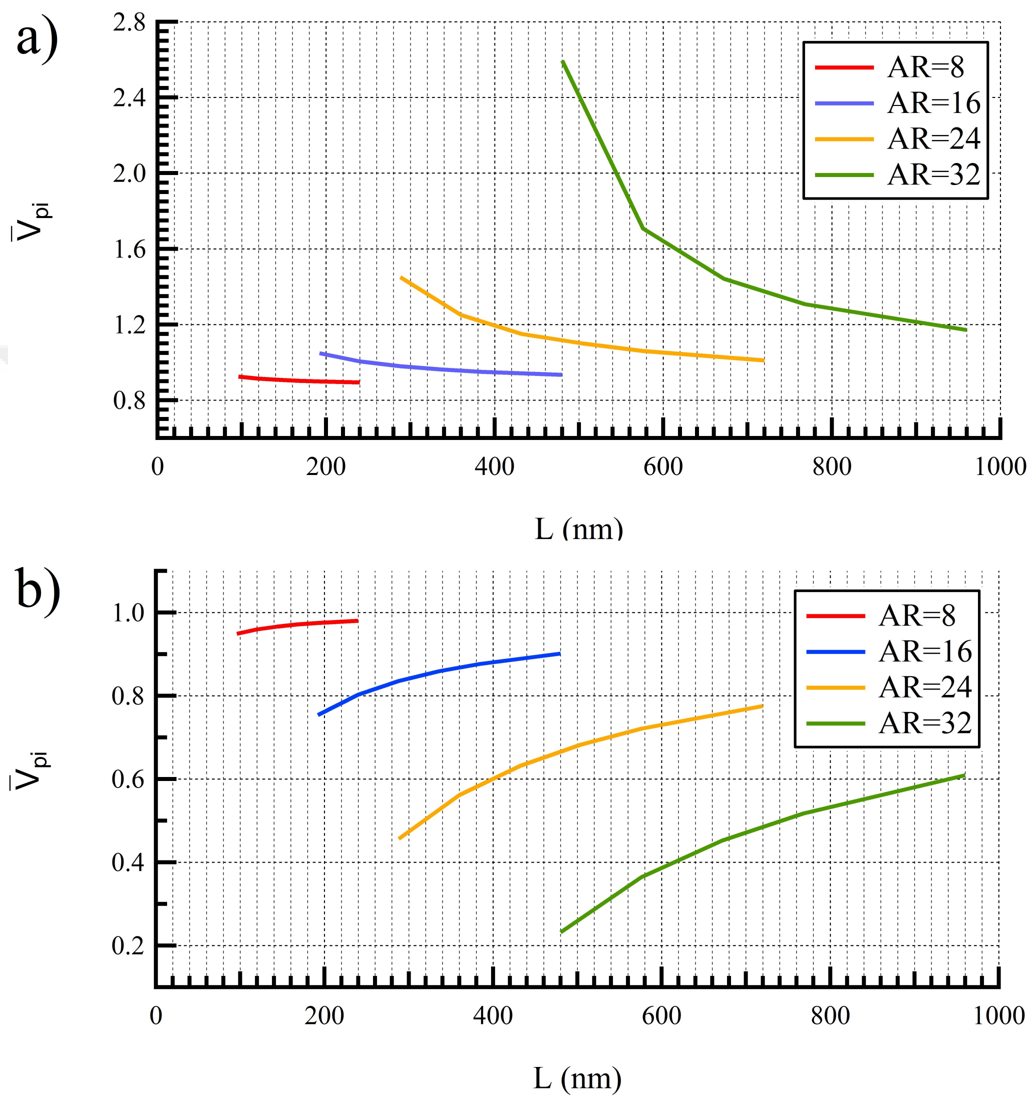

Figure 2.7: $\bar{V}_{pi}$ vs. L for various ARs for case 2 in: a) fixed-fixed b) cantilever boundary conditions

In figure 2.7.b, the effect of increasing length in cantilevers in various aspect ratios on the surface stress contribution to the calculated V_{pi} is demonstrated. It is observed that as the aspect ratio increases, the length parameter has more effect on the calculated V_{pi}.

The effect of changing aspect ratio on the normalized pull-in voltage in fixed-fixed beams for different surface area to volume ratios are demonstrated in figure 2.8.a.

One obvious conclusion from this figure is that as the surface area is increased, the contribution of the surface effects are increased as well. However, this increase is less in smaller aspect ratios. For aspect ratio of 32, not including the surface effects can lead to as much as double value of the actual pull-in voltage.

As with the fixed-fixed beams, the surface parameters contribution to pull-in calculation is minimized for smaller aspect ratios as shown in figure 2.8.b. In this case, ignoring the surface effects will lead to under-calculation of the pull-in voltage, and as the surface area to volume ratio increases, the deviation from the actual pull-in value will increase. For the case of aspect ratio of 32, the calculated pull-in voltage, when ignoring the surface stress will reach only 0.2 of the pull-in when surface effects are included. So far different methods are proposed to include the surface effect on the operation of NW switches. The Euler beam theory is used to implement the surface effects including residual surface stress and surface elasticity on the pull-in instability of nanobeams (Ma et al., 2010). The geometrically non-linear Euler beam model is introduced to study the pull-in voltage of NW switches (Wang and Wang, 2014), while the surface elasticity effect on the response of beam switches can be modeled by a modified continuum approach (Fu and Zhang, 2011). All those studies present a higher V_{pi} with including the surface effect. Similar behavior is found in figure 2.5. Furthermore, the geometrical effect on the surface effect is presented through figure 2.6-2.8. Although the previous works study the size effect on the pull-in response of nanobeams, the influence of boundary condition is investigated here for NW switch further to geometrical effects.

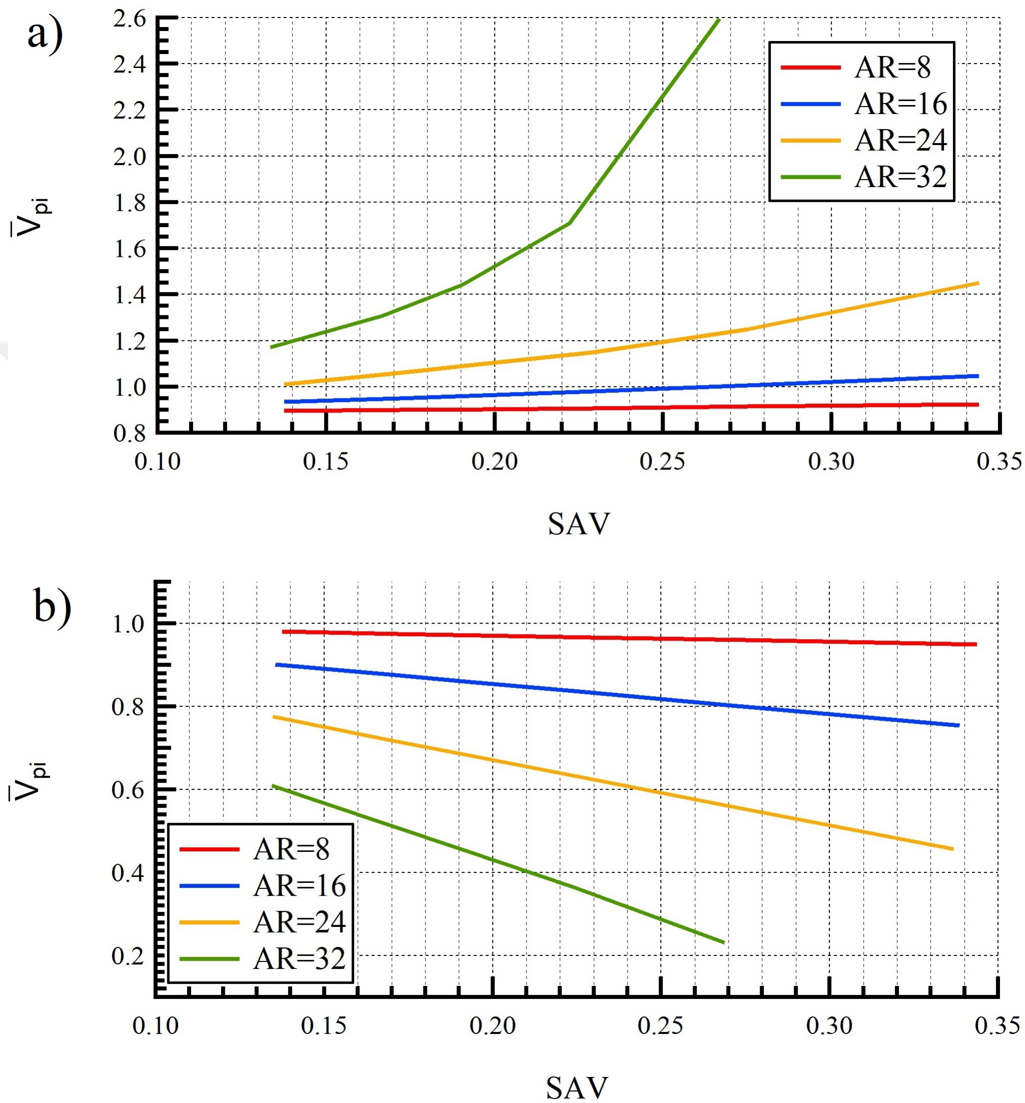

Figure 2.8: $\bar{V}_{pi}$ vs. SAV for various ARs for case 2 in: a) Fixed-fixed b) cantilever boundary conditions

2.6 Conclusion

In this chapter, a numerical model was developed to study the surface contribution to the electromechanical behavior of the SiNWs with various geometries and boundary conditions. It was observed that AR plays an important role in determining the extent of the surface stress effect. In low ARs, NWs with various thicknesses had the same $\bar{V}_{pi}$, and as the AR increased, the pull-in values for different thicknesses diverted from each other. The surface effect reduced the V_{pi} for fixed-fixed beams, whereas in cantilevers it increased the pull-in.

Increasing NW length with constant AR decreased the $\bar{V}_{pi}$ for fixed-fixed NW while increasing it for the cantilever boundary condition. In both cases, the effect of changing length in a small AR was insignificant. Thus once more it was concluded that AR is a better independent parameter to model the surface effect in NWs. It was also shown that, this size dependency appears when surface area to volume of a feature increases.

Chapter 3

FABRICATION OF ULTRA-THIN SILICON NANOWIRES

3.1 Overview

This chapter focuses on the fabrication of nanowire with high aspect ratio. The previous chapter explored the relation between pull-in voltage and physical properties of the NW switches through finite element analysis (FEA). This chapter is the link between numerical works and the characterization. Tests mostly has been carried out on micro-scale devices, since there are many difficulties in the way of fabricating nanodevices. In the following chapter, field-emission scanning probe lithography (FE-SPL) in combination with cryogenic etching is introduced to overcome the shortcomings of the available fabrication methods.

NWs are patterned on large micro-scale electrode pads on silicon-on-insulator (SOI) substrates with AZ Barli resist by FE-SPL. Fabrication process is followed by anisotropic cryogenic etching of SOI substrate. In this study, SiNWs with a critical dimension of 30 nm are integrated with electrostatic electrodes and gap distance of 45 nm.

3.2 Introduction

Due to their interesting electrical and optical properties, silicon nanowires have attracted attention as an important building block for complex sensing and actuation devices (Huang et al., 2001; Xia et al., 2003; Law et al., 2005; Kind et al., 2002; Garnett and Yang, 2010; Li et al., 2003a). The first SiNW has been fabricated in 1998 (Nasr and Alaca, 2018) and many other methods have been proposed afterwards. These methods can be divided in to two main categories: Top-down and bottom-up techniques. Top-down techniques consists of lithography methods that transfers the pattern to the photo-resist and then to the substrate by etching processes (Bolten et al., 2011; Cleland and Roukes, 1996; Allain et al., 2012; Tasdemir et al., 2015). On the other hand, the nanofeature is grown on the substrate through selected chemical reactions in bottom-up techniques (Lu and Lieber, 2010; He et al., 2005; Hu et al., 1999; Goldberger et al., 2006; Hochbaum et al., 2005; Law et al., 2004). The suitable choice of method depends on the application. In the following, the advantages and disadvantages of each of these techniques will be discussed.

One very established method of top-down techniques is photolithography, in which light is used to transfer patterns from a mask to a photo-resist on the substrate. This method is suitable for large-scale manufacturing due to its high throughput capability. Other top-down methods are e-beam, nano-imprint and scanning probe lithography. Of disadvantages of this category is the usually flawed geometry after etching process (Biswas et al., 2012). To overcome this issue advanced lithography techniques yet has to be introduced.Generally, down sizing is a challenge for top-down methods although their assembly and integrated circuits (IC) integration is more favorable comparing to bottom-up methods.

Bottom-up fabrication methods such as atomic layer disposition (ALD), sol gel nanofabrication and molecular self assembly usually provide the ability to construct advanced devices without predefining detailed masks. Moreover, fabricating nanodevices through these method will lead to no waste process, which is very desirable in mass fabrication. In contrast to top-down methods, in bottom-up techniques perfect geometry is possible after fabrication through simple processes. However, these methods are not mature enough for manufacturing purposes. Moreover, NWs fabricated through these methods are difficult to align and integrate (Erdem Alaca, 2009).

In efforts to fabricate SiNWs, Lieber and Morales (1998) introduced a combination of a laser ablation method and vapor-liquid-solid (VLS) growth for the synthesis of a semiconductor NW. VLS growth is a popular fabrication method of nanowires and first has been introduced by Wagner and Ellis (1964). In this method vertical growth of silicon is achieved by locating a very low temperature alloy droplet on silicon substrate, then expose it to a vapour. The VLS growth have been reported to be applied to substrates of various materials such as BeO, GaAs and SiC (Wagner and Ellis, 1964).

Another prominent bottom-up method in NW fabrication is ALD. This method was first introduced by Suntola (1989) and involves growing a very thin atomic-scale film over the substrate. Initially, ALD had the disadvantage of a very slow growth which later improved and now is used in semiconductors mass fabrication as well (Kim et al., 2009).

Due to possibility of performing parallel processes, photolithography is a popular top-down fabrication method. Rogers et al. (1997) were able to fabricate 100 nm features using photolithography with elastomeric phase masks. On the other hand, e-beam lithography is superior to photolithography techniques since it does not suffer the light diffraction limitation and can be used to fabricate smaller scale features. However, this method has a low throughput and is challenging to implement for features with less than 20 nm dimensions. Juhasz et al. (2005) has reported fabrication of silicon nanowires of widths 100-200 nm through e-beam lithography and they propose an electrochemical size reduction technique to scale down the width to 10 nm regime. Another high resolution technique is the SPL fabrication. This method can be categorized in scanning tunnelling microscopy (STM), atomic force microscopy (AFM), or near-field scanning optical microscopy (NSOM). Although it is a high resolution technique, the low throughput capability of the SPL refrains it from commercial manufacturing, besides its generally an expensive process. Hu (1998) has fabricated silicon and metal nanowires of 20 nm on bilayer resists resolution using mechanical AFM.

Recently, a field- emission scanning probe lithography (FE-SPL) is developed (Lenk et al., 2018) for the fabrication of nanoscale devices for the fabrication of single electron transistor (Lenk et al., 2019) and optical devices (Aydogan et al., 2018). The low energy emitted from secondary electrons in FE-SPL – in contrast to available technologies – can be used to minimize the proximity effects for high resolution patterning outcome at ambient temperatures and room conditions. Enabling atomic force microscopy imaging, FE-SPL patterning can be monitored for further modifications (Lenk et al., 2018).

In the subsequent subsection, the principles of the FE-SPL will be explained. Then, design parameters of the NWs will be presented in the next part. The AFM images of the NWs will be provided after describing the fabrication process.

3.2.1 Field-emission scanning probe lithography mechanism and applications

FE-SPL setup used at our lab is demonstrated in figure 3.1. The basic working principle of this tool is the electron emission from the thermomechanically actuated, piezoresistive cantilever tip. One such tip is shown in figure . This emission follows Fowler-Nordheim relation and result of simulations on the FE-SPL tips are presented in (Lenk et al., 2017). Based on the simulations, the tips diameter is an important factor in defining the field strength away from the tip to the sample surface and pattern quality. There is a coarse positioning system which enables directing the sample to the desired point under the cantilevers tip through optical navigation. Moreover, the tip-sample distance (10-100 nm) is controlled by a closed-loop feedback system and depends on the exposure parameter, i.e. tip-sample current divided by lithography speed.

The scanning area is a 10×10 μm^2 space. However, a step and repeat functionality is provided to enable lithography on larger area. The low energy emitted from the secondary electrons ($<$ 10 eV), unlike previous techniques, help to eliminate the proximity effects and thus makes patterning features with single digit nanometer critical dimension (CD) possible (Zoellner et al., 2018). The electric field covers the 10-100 nm tip-sample distance which is much smaller than the mean free path of the electrons in the air, therefore although to have more control over ambient condition our SPL machine is placed in the cleanroom, it can be utilized in the normal laboratory conditions. This and the fact that no vacuum condition is needed for SPL operation are great advantages, since a cleanroom is an expensive facility.

Another improvement that makes FE-SPL superior to its predecessors is the closed loop lithography system which enables the inspection of the sample, before and after the lithography thus better overlay alignment with the same cantilever and configuration. This also provides an optimum mix and match ability with other lithography methods such as e-beam (Kaestner et al., 2013) and nanoimprint lithography (Lenk et al., 2019) which is crucial to overcome the low throughput capability of the FE-SPL.

When the features dimension is in extreme nano dimension, transferring the pattern to the silicon is a delicate task. The reactive ion etching (RIE) is an isotropic process, thus not suitable for this dimension. However, if RIE is performed at cryogenic temperatures the etching will be anisotropic. SF_6/O_2 gases are classically used for cRIE of silicon. Si, F and O_2 gases produce polymeric SiO_xF_y at cryogenic temperatures which will protect the silicon from the etchant. This method provides the possibility to precisely transfer the patterns with high aspect ratios and less than 20 nm dimensions.

Using the FE-SPL and cryogenic etching single electron transistors (Lenk et al., 2019) and optical nano devices (Aydogan et al., 2018) has been fabricated. Our study will present the capabilities of this fabrication method to create nano-scale active features.

3.3 Fabrication process and method

Fabrication is carried out on a silicon-on-insulator (SOI) substrate with a 14-nm-thick device layer and a 25-nm-thick buried oxide layer. Microscale contact pads and areas for device definition and electrical measurements has been patterned and etched on the substrate through photolithography (figure 3.5). The substrate is then coated with 10 nm thick AZ Barli, for deep-nano-scale pattern transfer.

NWs with lengths 2-4 μm, widths 40-100 nm and an average gap of 50 nm between NW and electrodes has been patterned in positive tone through FE-SPL. The lithography parameters are mostly around: 100 V bias voltage, 13 pA current, and 0.2 $\mu m/s$ lithography speed. The isolation of the patterned NWs on electrode pads from

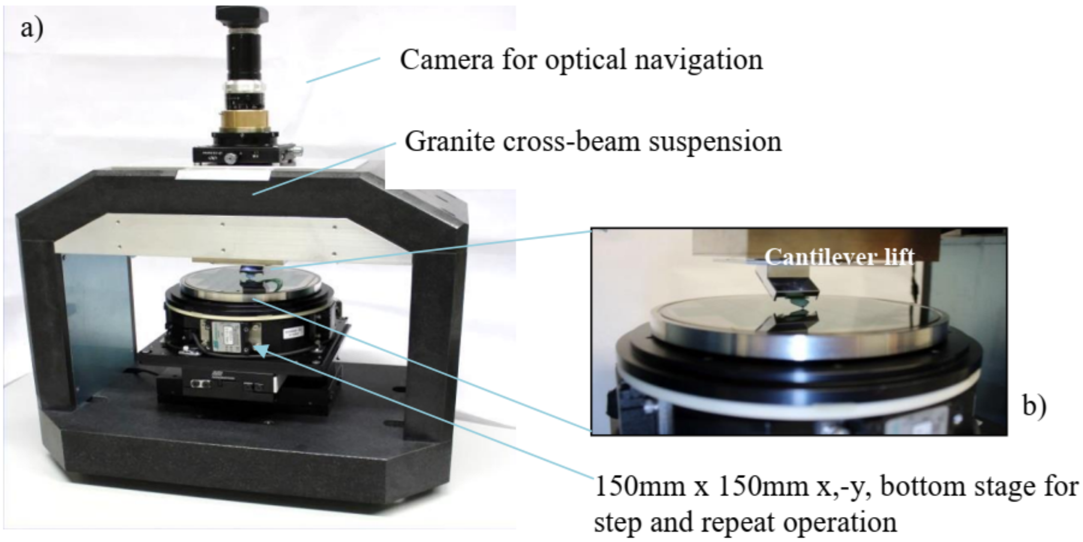

Figure 3.1: FE-SPL setup used for fabrication(Lenk et al., 2017) .

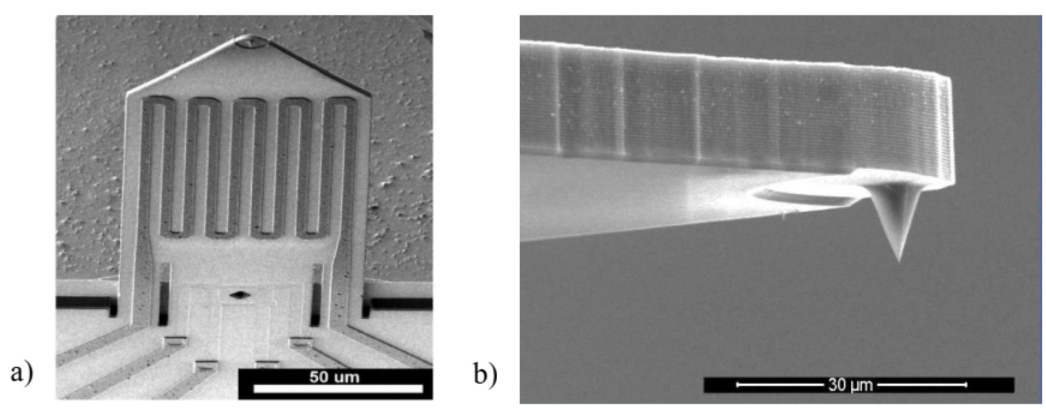

Figure 3.2: SEM images of the silicon cantilever tip(Lenk et al., 2017).

surrounding electrical connections are carried out through focused ion beam.

In the following fabrication step, a reactive ion etching (RIE) process is performed for 20 seconds under 6 mTorr pressure, at a cryogenic temperature of -120 °C in an Oxford Instruments Cobra 100 ICP etcher, where SF_6/O_2 gases are used for the anisotropic etching of Si.

As mentioned before, the performance of the FE-SPL patterns depends on tip radius, environmental conditions, patterning parameters (V voltage, A current, S lithography speed) and lithography and scanning feedback loop parameters ($I\&P$); therefore, calibration is necessary to have a quality outcome. For this purpose, a feature is patterned multiple times with changing the parameters as is seen in figure 3.3. This figure provides an instance of calibration for a certain tip, and the calibration must be done whenever any condition is changed. Calibration should be done for each of the lithography parameters. A high quality result is defined both by observation and current signal. It is preferable that the current amplitude remains in $\pm 2pA$ (figure 3.4).

3.4 Results and discussion

Patterning of NWs aligned between two electrodes with minimum feature size is the main objective in fabrication process. Figure 3.6 shows the AFM image of a patterned NW with 2 μm length and 110 nm with surrounded by two electrodes. The AFM profile measurement indicates an average gap of 45 nm between NW and electrodes (Figure 3.6. (b)). This pattern is obtained under FE-SPL voltage of 100 V, current about 13 pA and scanning speed of 0.3 $\mu m/s$. Increasing voltage to 80 V in a scanning speed of 0.2 $\mu m/s$ enables patterning of a NW with length of 3 μm and width of 145 nm (Figure 3.10). The reduction of the lithography speed in FE-SPL increases the gap between NW and electrodes to 55 nm. Further reduction on the NW width to 95 nm and increase on length to 4 μm is obtained through using the same FE-SPL parameters as shown in figure 3.11.

Figure 3.12 demonstrates the patter of a NW with length of 2 μm and width of 110

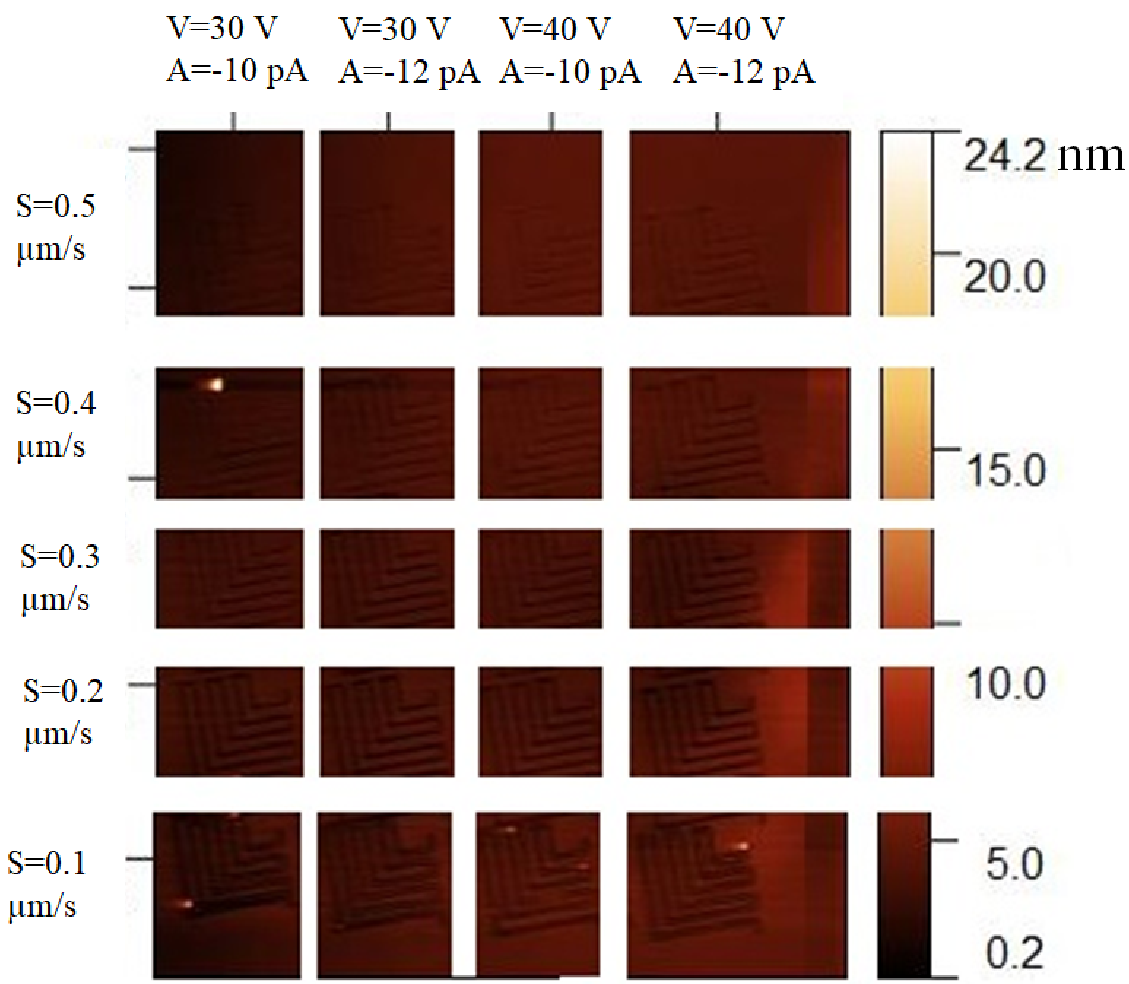

Figure 3.3: Calibrating voltage, current and lithography speed

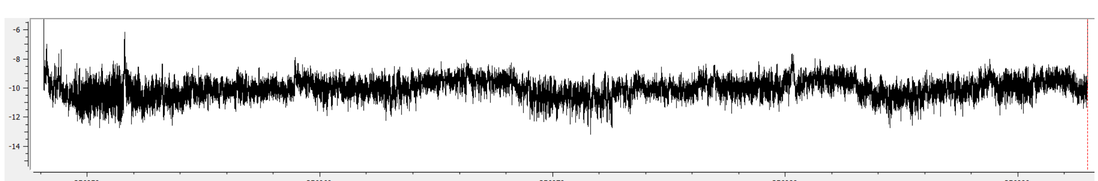

Figure 3.4: A reasonable lithography current signal for A=12 pA

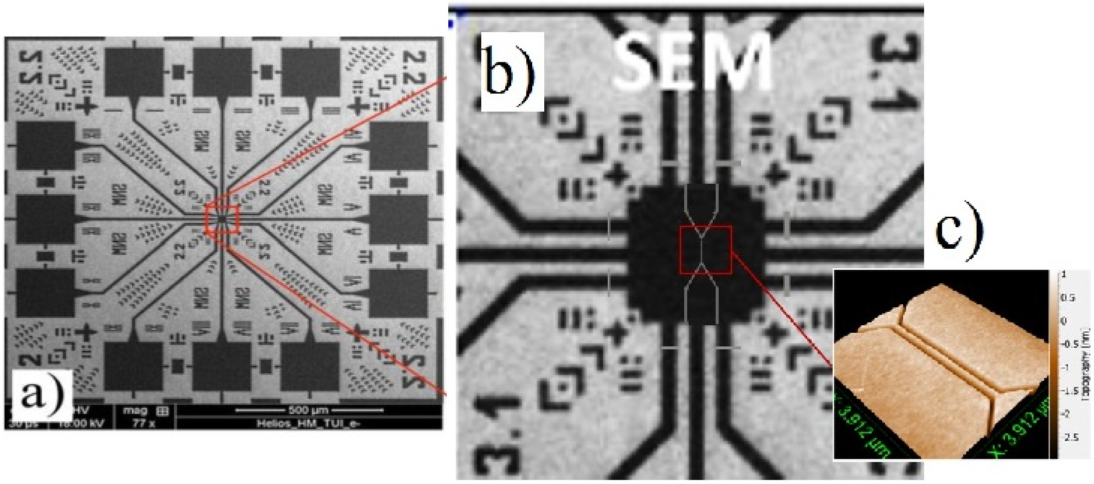

Figure 3.5: SEM image of substrate a) Sample layout through photolithography b) device positioning illustration c) AFM image of a NW

nm. A gap of 45 nm between NW and electrodes is obtained through using FE-SPL voltage of 100 V, current of 13 pA and scanning speed of 0.3 $\mu m/s$. Likewise, Figures 3.13 and 3.14 show the 3D scanning images of the NWs in figures 3.10 and 3.11 respectively.

Here, the mix and match ability of the FE-SPL is highlighted through fabricating ultra-thin silicon NWs. The easy switch between exposure and AFM modes and coarse positioning enable precise overlay alignment on the previously defined contact pads without the need to marking. NWs are patterned and then isolated from the redundant connections to alleviate electrical noises by stitching. The ambient conditions were strictly under controlled and kept stable at relative humidity of $30\% \pm 10\%$ and temperature of $21 \pm 10\%$.

3D images of the working area before and after lithography for NW with length 2 μm are shown in figure 3.12. Both 3D and 2D imaging is possible in our FE-SPL setup. In the pre-lithography working area an abrupt elevation can be noticed. Since the probe scans the area horizontally, the field is blocked in the vicinity of the hill and it looks as non-existent. Changing the scanning angle may include more area around the defect, however the main aim here is to clearly present the NW. 45 degree alignment of the scanning lines and feature has been reported to reduce the imaging errors (Lenk et al., 2017). The depth of the pattern is around 14 nm. The geometrical parameters and cross sectional profile for this NW is described in figure 3.6. The software accompanying the FE-SPL tool, provides a high resolution AFM image which then is processed to extract the geometry parameters and cross section profiles. The line edge roughness (LER) has been reported as sub-nm values (Zoellner et al., 2018). Figures 3.11 and 3.14 shows 2D and 3D images of NW with length 4 μm. Since the FE-SPL performance is dependent on many parameters such as surface conditions and ambient condition a small hill is seen in the gap line. However, due to the very small diameter of the flaw it will be eliminated after etching.

Figure 3.7 shows a cantilever-type structure patterned using FE-SPL. The thick gap around the cantilever assures that the etchant will reach the Si. Furthermore, to make sure that there is enough space for the etchant around the cantilever, the gap has been increased. In figure 3.8 the gap has been raised to 250 nm with voltage of 80 V, current of 13 pA and dose of $0.5\mu m/s$. The length of the cantilever is 1 μm with a width of 52 nm. Further increasing the gap to 550 μm results in the feature shown in figure 3.9. A summary of the patterned features and their lithography parameters is provided in table 3.1.

3.5 Operation of nanowire electromechanical devices

The operational response of fabricated NWs is calculated in this section. Resonance frequency and pull-in voltage are estimated for Si NWs listed in table .... The resonance frequency is estimated by using the analytical equation of

$$f_n = \frac{k_n^2}{2\pi L^2}\sqrt{\frac{EI}{\rho A}} \tag{3.1}$$

$k_n = (n\pi + \pi/2)$ is the constant values related to the mode (Bao, 2005). Further to the resonance frequency analysis, pull-in voltage is calculated based on the numerical method developed in the previous chapter. The pull-in voltage is calculated for two

Table 3.1: Summary of dimensions pattern for NWs with different boundary conditions

NW length (μm)	NW width (nm)	Gap (nm)	Boundary condition	FE-SPL parameters		
				Voltage (V)	Current (pA)	Speed ($\mu m/s$)
2	110	45	Fixed-Fixed (figure 3.6)	100	13	0.3
2	200	40	Fixed-Fixed	80	12	0.2
2	40	30	Fixed-Fixed	100	13	0.3
2	107	48	Fixed-Fixed	100	13	0.3
2	120	65	Fixed-Fixed	100	13	0.3
3	145	55	Fixed-Fixed (figure 3.10)	80	12	0.2
3	100	50	Fixed-Fixed	100	13	0.3
3	155	50	Fixed-Fixed	80	12	0.2
4	95	55	Fixed-Fixed (figure 3.11)	80	12	0.2
4	120	45	Fixed-Fixed	80	12	0.3
4	220	45	Fixed-Fixed	80	10	0.3
1	55	140	Fixed-Free (figure 3.7)	80	13	0.3
1	52	250	Fixed-Free (figure 3.8)	80	13	0.3
1	55	550	Fixed-Free (figure 3.9)	100	20	0.3

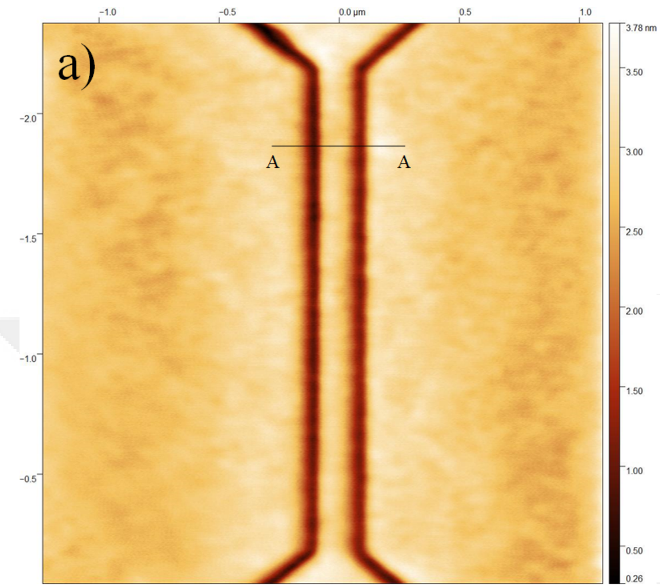

c)

Parameter	Value
Width	110 nm
Gap	45 nm
Length	2 μm
Voltage	100 V
Current	-13 pA
Speed	0.3 μm/s

b)

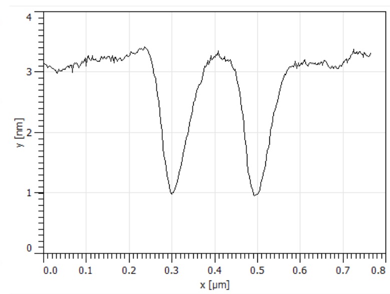

Figure 3.6: Properties of the $2\mu m \times 110nm \times 14nm$ NW a) 2D AFM image b) A-A profile c) geometry and lithography parameters

Parameter	Value
Voltage	80 V
Current	-13 pA
Speed	0.3 $\mu m/s$
Dose	-433.33 nC/cm
RH	~ 25
Temperature	~ 21

Line	Value (μm)
1	0.141
2	0.146
3	0.908
4	0.123
5	0.127

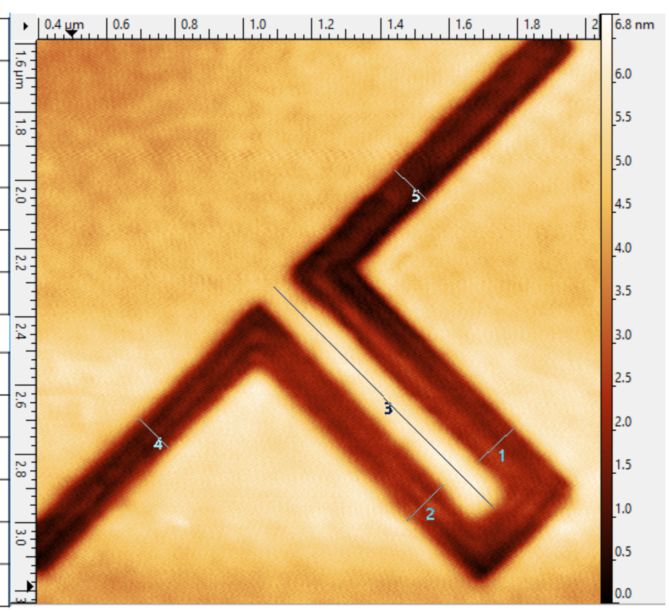

Figure 3.7: AFM image and Properties of the $1\mu m \times 55nm \times 14nm$ cantilever

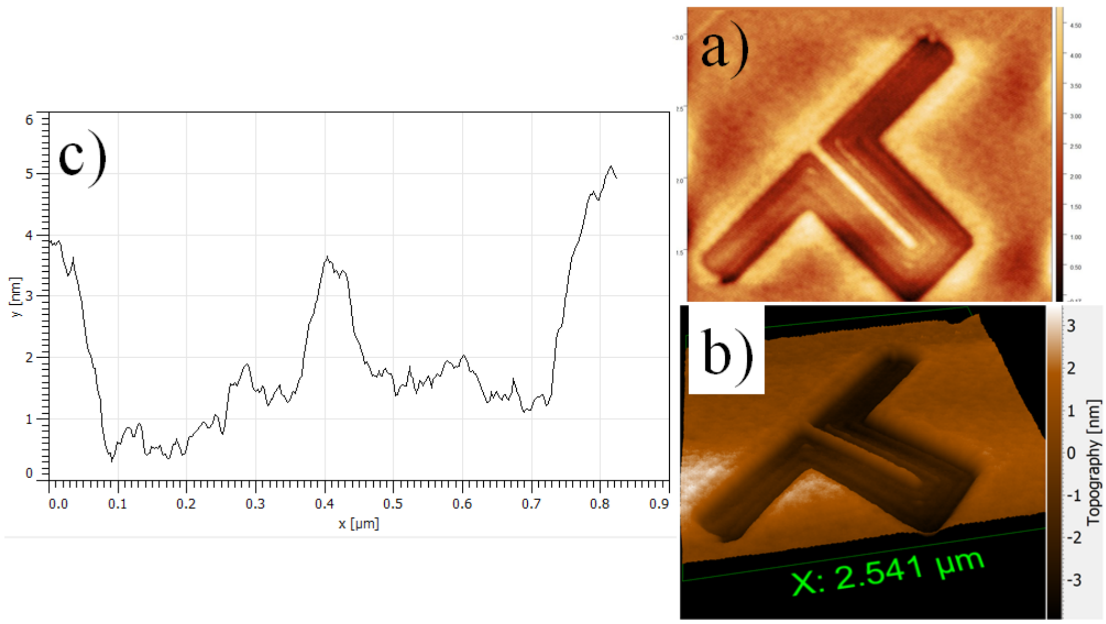

Figure 3.8: AFM image and Properties of the $1\mu m \times 52nm \times 14nm$ cantilever a) 2D AFM image b) 3D image c) cross section profile

Parameter	Value
Voltage	100 V
Current	-20 pA
Speed	0.3 $\mu m/s$
Dose	-600 nC/cm
RH	~ 30
Temperature	~ 21

Line	Value (μm)
1	0.450
2	0.550

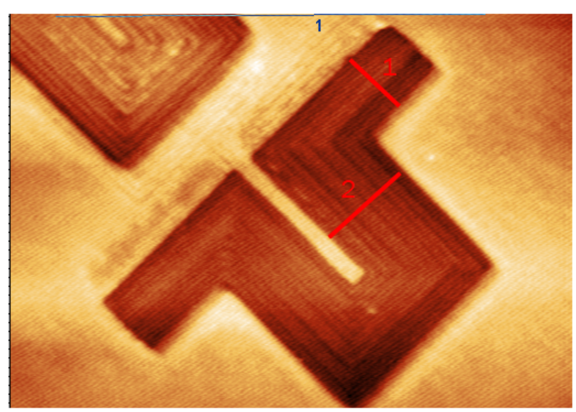

Figure 3.9: AFM image and Properties of the $1\mu m \times 55nm \times 14nm$ cantilever

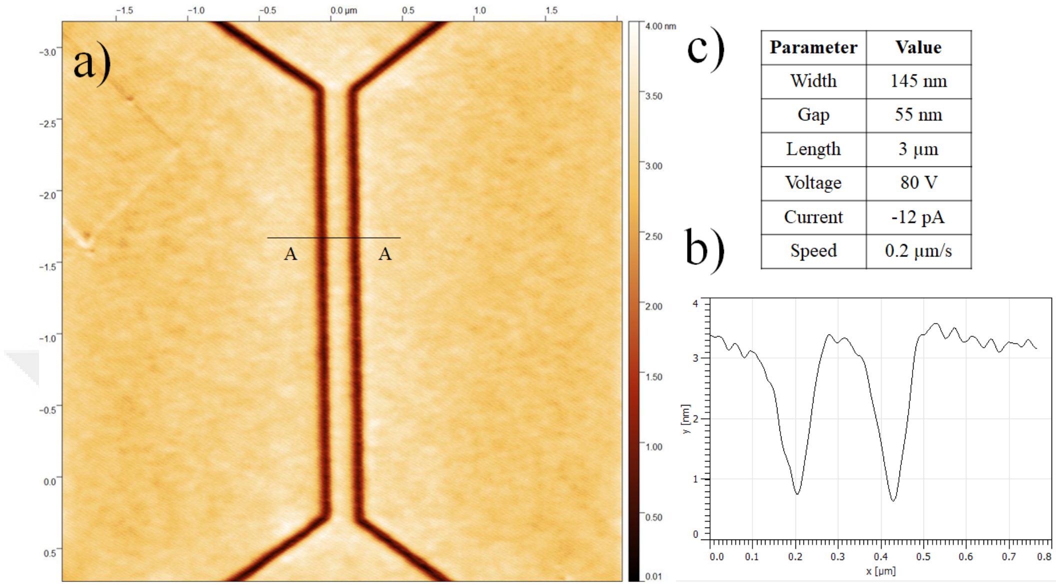

Parameter	Value
Width	145 nm
Gap	55 nm
Length	3 µm
Voltage	80 V
Current	-12 pA
Speed	0.2 µm/s

Figure 3.10: Properties of the $3\mu m \times 145nm \times 14nm$ NW a) 2D AFM image b) A-A profile c) geometry and lithography parameters

difference physics of case 1 and case 4 listed in table 1.2. In case 1, electric softening and the surface effect are considered, while case 4 is neglecting surface effect and electric softening.

The operational behavior of patterned Si NWs as a resonator or a mechanical switch is listed in table 3.2.

Results in the table 3.2 show a resonance frequency on a range of 7 to 30 MHz. A pull-in voltage about 3 to 85 V is estimated through considering the surface effect and electric softening, while the pull-in voltage is about 11 to 198 V for a simple model considering constant gap and without surface stress. The maximum difference between calculated pull-in voltage through case 1 and case 4 is obtained for NW with length of 2 μm and width of 200 nm, while the NW with length of 2 μm and width of 40 nm has the lowest difference between pull-in voltage models.

Table 3.2: The resonance frequency and pull-in voltage of patterned Si NWs.

NW Length (μm)	NW width (nm)	Gap (nm)	Resonance frequency		Pull-in voltage	
			Mode 1 (MHz)	Mode 2 (MHz)	Case 1 (V)	Case 4 (V)
2	110	45	30.7964	667.0156	40.641	96.5467
2	200	40	30.7964	1212.7556	84.223	198.3637
2	40	30	30.7964	242.5511	3.796	11.5241107
2	107	48	30.7964	648.8242	42.915	102.0384
2	120	65	30.7964	727.6534	80.577	190.9718
3	145	55	13.6872	390.7768	36.957	87.7485
3	100	50	13.6872	269.5012	17.979	43.5611
3	155	50	13.6872	417.7269	35.467	84.0624
4	95	55	7.6991	144.0147	10.449	26.1768
4	120	45	7.6991	181.9133	11.344	27.5019
4	220	45	7.6991	333.5078	28.897	68.2737

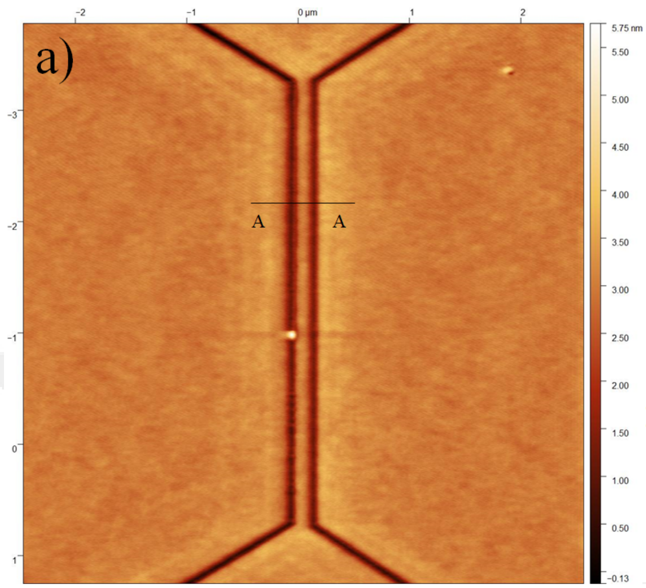

c)

Parameter	Value
Width	95 nm
Gap(left)	55 nm
Length	4 µm
Voltage	80 V
Current	-12 pA
Speed	0.2 µm/s

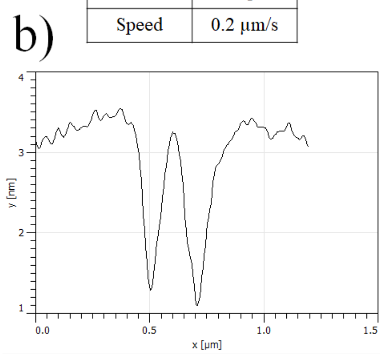

Figure 3.11: Properties of the $4\mu m \times 95nm \times 14nm$ NW a) 2D AFM image b) A-A profile c) geometry and lithography parameters

3.6 Conclusion

The potential to merge the FE-SPL method in a mix and match technique for fabricating ultra-thin SiNWs was demonstrated in this chapter. The SiNWs with a critical dimension of 30 nm were integrated with electrodes. A minimum gap of about 45 nm between SiNWs and electrodes was obtained. The use of FE-SPL addresses the existing challenge in available techniques on alignment of nanofeatures with a critical dimension below 50 nm.

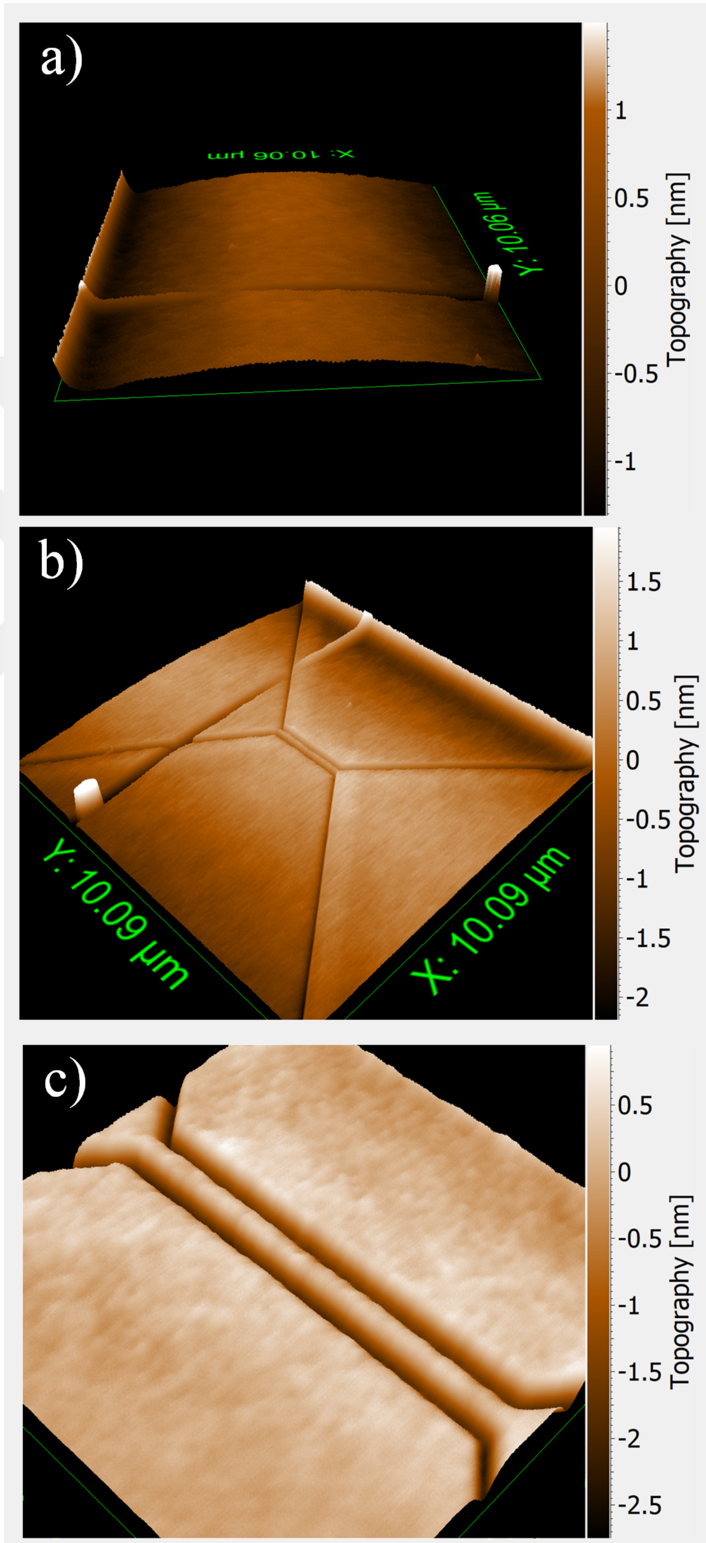

Figure 3.12: 3D AFM images of working area for $2\mu m \times 110nm \times 14nm$ NW a) pre-lithography b) NW after lithography c) close-up of the NW

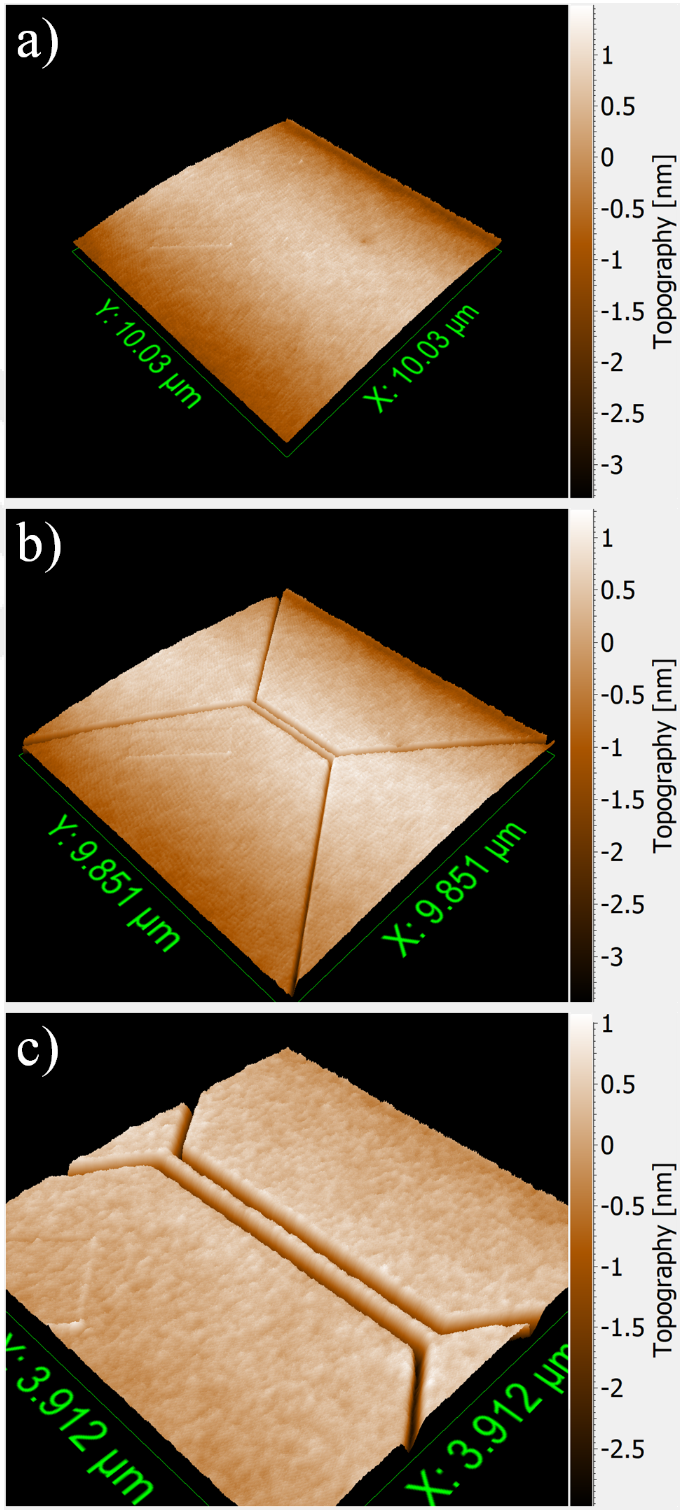

Figure 3.13: 3D AFM images of working area for $3\mu m \times 145nm \times 14nm$ NW a) pre-lithography b) NW after lithography c) close-up of the NW

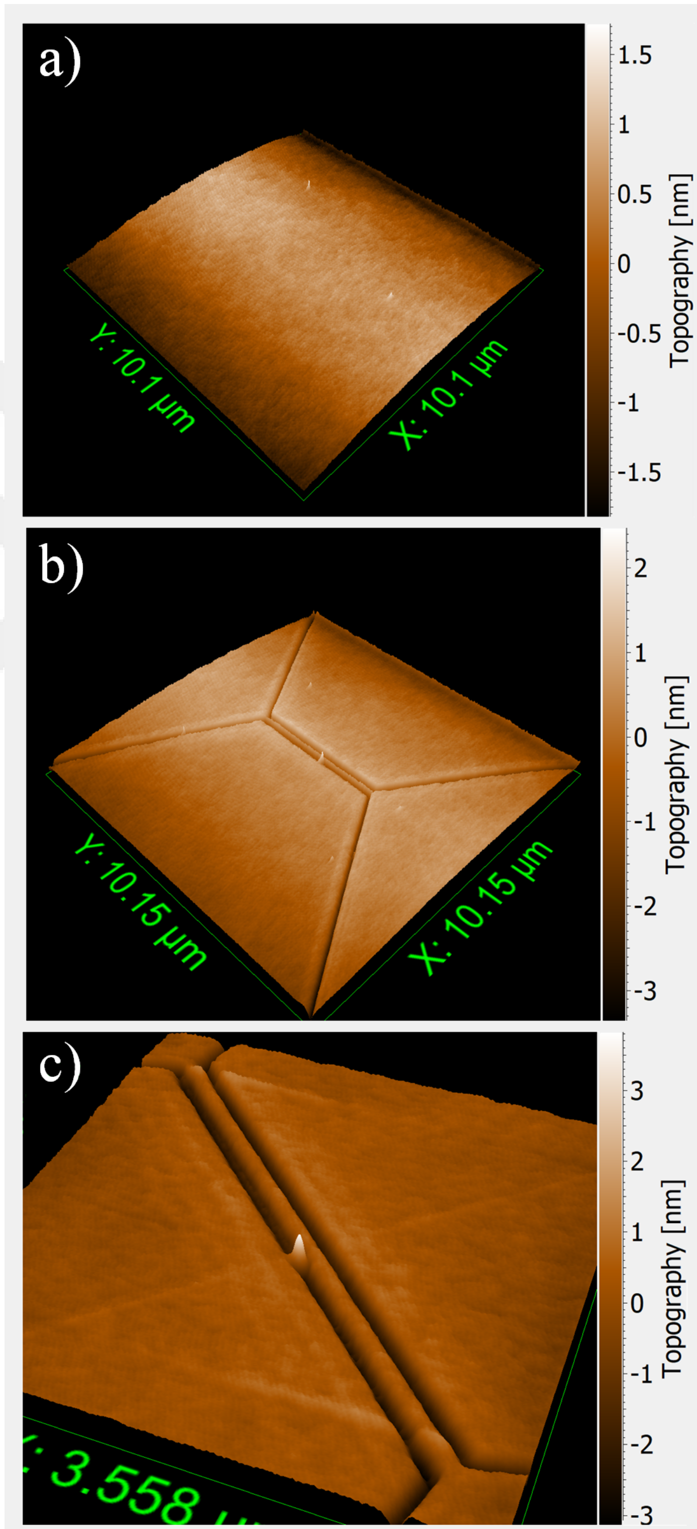

Figure 3.14: 3D AFM images of working area for $4\mu m \times 95nm \times 14nm$ NW a) pre-lithography b) NW after lithography c) close-up of the NW

Chapter 4

SURFACE CHARACTERIZATION OF SILICON NANOWIRES

4.1 Overview

Now that the numerical model and the NWs have been prepared, in this chapter, a model is proposed to extract the surface parameters of a SiNW. Characterization of SiNWs has been an ongoing research for years now. The surface contribution is studied using the surface elasticity and surface stress. Various values have been reported for these two parameters. An instance of contradictory values is provided in table 4.1. As is observed the values differ so much. However, still the numerical models are incapable of predicting the properties of NWs with enough precision. Pull-in voltage measurement is considered a high fidelity method to extract the surface properties and to enhance the current available models.

Table 4.1: Comparison of various values suggested for E_s and τ_0 for $< 100 >$ Si

reference	E_s (N/m)	τ_0 (N/m)
Fu and Zhang (2011)	-10.036	0.605
Yun and Park (2012)	-8.07	-0.88

4.2 Introduction

Extensive economic studies have forced on the semiconductor manufacturing industry to follow Moore's law [1]. Increasing the device density per area of integrated circuits requires downscaling. While understanding the electromechanical properties of nano-scale devices becomes a fundamental challenge for engineering design. Many experiments have been performed to analyze the micro and millimeter sized specimen; however, in nanoscale systems due to the order of the properties it requires advance technology and methods for characterization. Studies have shown that after a threshold in miniaturization, the mechanical properties of the materials become size-dependent (Nasr Esfahani and Alaca, 2019). This size-dependency has been studied both computationally and experimentally. A suitable characterization platform will take loading and measurement methods in meticulous consideration. The load should be applied in a well controlled manner and the measuring system should be synced in a way to enable recording such minuscule deflections associated with NEMS. Furthermore, aligning the NEMS device with the loading mechanism will have crucial impact on the result in that it defines the boundary condition of the system. Also providing a proper contact to the NW to capture and apply desired parameters is a critical step. The loading type is categorized as

- quasistatic
  - tension
  - compression
  - bending
- resonance

Recently, a pull-in instability method has been introduce by Sadeghian et al. (2009) for characterization purposes. The method is advantageous over bending tests in that the errors caused by applying voltage is much less and the structure is not affected by mass-loading. Moreover, the devices reactions is observed and analyzed much easier than say AFM bending or resonance methods. The experiment can also be done using common electrical test equipment and microscope.

Further to experimental investigations, several computational models are proposed to include size dependency into the mechanical behavior of NWs. As an analytical method, He et al. (2008) introduced a solution to modified Young-Laplace model to describe the change in Young's modulus. Song et al. (2011) improved their model by including initial surface stress and solved the model numerically. Miller and Shenoy (2000) also proposed a simple model to relate the size-dependent changes in mechanical properties to the geometry and a surface parameter. However, the computational models still have deficiencies to predict the size-dependent mechanical properties accurately (Nasr Esfahani and Alaca, 2019). Closing the gap between the experimental and computational studies is the main objective of this chapter. The approach to measure pull-in voltage of NWs will be discussed first. Then, the numerical algorithm to use pull-in voltage for surface properties of Si NWs will be described.

4.3 Methodology

In this study, an Agilent B1500A semiconductor device analyzer is used to extract the pull-in voltage of the NWs fabricated in the previous chapter. No vacuum condition is necessary for pull-in measurements. Figure 4.1 shows the schematic to the measurement setup including the semiconductor analyzer, electric connections and device. The connections will be made through wire-bonding the pads on a PCB board. A voltage difference is forced through port B to the electrode lying along the length of the NW. an electrical force will forces the NW to bend and when instability happens a current will be abruptly flowed and captured. The voltage precisely before the current is established is the V_{pi}.

After having the pull-in voltage for a range of size, a numerical analysis should be used to link the pull-in voltage to the mechanical properties of Si NWs. To extract the surface parameters, τ_0 and E_0, a set of NWs with constant cross section and different lengths is fabricated. Therefor in equation 2.3, $(EI)^*$ and P^* will be constant. By defining a constant parameter of $\alpha = P^*/(EI)^*$, then the nondimensional surface effect factor can be written as $\eta = \alpha L^2$. Noticing that by using the parallel plate capacitor estimation 2.18, the pull-in voltage and Young's modulus can be related as

$$\frac{V_{exp,pi}^2 - V_{0,pi}^2}{V_{0,pi}^2} = \frac{E_{eff}^{exp} - E_0}{E_0} \tag{4.1}$$

In equation 4.1, $V_{exp,pi}$ is the experimentally measured pull-in voltage, $V_{0,pi}$ is the pull-in voltage calculated from the developed numerical model when no surface effect is considered, E_{eff}^{exp} is the effective Young's modulus of the NW from the experiment. Rephrasing equation 2.3, equation 4.1 can relate pull-in voltage to an equation where only $\frac{\sqrt{\alpha}L}{4}$ parameter dependent on geometry and surface parameters is unknown, as

$$\frac{V_{exp,pi}^2 - V_{0,pi}^2}{V_{0,pi}^2} = \gamma = f(\frac{\sqrt{\alpha}L}{4}) = \frac{\beta}{[1 - \frac{tanh(\frac{\sqrt{\alpha}L}{4}))}{\frac{\sqrt{\alpha}L}{4}}]} - 1 \tag{4.2}$$

Where in equation 4.2 $\beta = \frac{(EI)^*}{3E_0 I}(\frac{\sqrt{\alpha}L}{4})^2$. To extract the surface parameters the following algorithm is suggested:

Algorithm to extract surface parameters from the pull-in measurements

1. assign α_0 from literature and γ values using the experimental and numerical results

2. plot $(\gamma + 1)$ versus $\frac{\sqrt{\alpha_0}L}{4}$

3. fit a line to the scattered data and extract β_1

4. From β_1 calculate α_2

5. Compare α_0 and α_2. If they are identical got to next item, if not go to 2 and repeat

6. Repeat 1-5 for another set of NWs with constant cross section and calculate α'

7. With two α, there are now a set of equations with two unknowns. Solve for τ_0 and E_s

Therefore, the actual surface parameters for SiNWs is extracted by combination of the developed model in chapter 1 and experimental pull-in measurements from NWs of chapter 2.

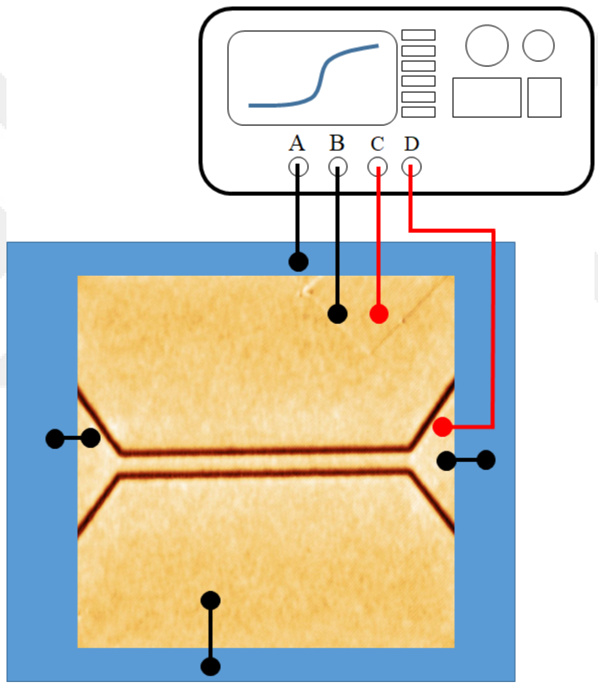

Figure 4.1: Schematic of the measurement setup, the blue background is the PCB

4.4 Conclusion

A method was proposed for surface characterization of SiNWs based on pull-in measurements. This method combined the numerical scheme developed in chapter 2 and the electromechanical properties of the NWs in chapter 3 to extract the surface parameters based on the algorithm in chapter 4. A numerical method was fully developed following the fabrication of Si NWs with high aspect ratios. Measurements are to be carried out in the next step. To extend this research, resonance frequency measurements will be carried out to characterize the surface parameters.

4.4.1 Remarks

In addition to the pull-in voltage measurements, an experiment on the capacitance will be carried out. Due to large contact pads and a very thin oxide layer between the metal and the handle layer, a parasitic capacitance will be formed in the pad called the depletion zone (Yuan and Liou, 2013). Since the capacitance between the NW and the electrode will be very low, this parasitic capacitance will affect our capacitance measurements and make it difficult to quantify the device performance. However, This phenomena will not interfere with pull-in voltage measurements. To neutralize the effect on the final capacitance measurement, one way is to experiment with samples without the NW and measure the parasitic capacitance. The model in this chapter will be modified by interpreting the depletion zone created in the NW.

Chapter 5

CONCLUSION

In the current project, we were aiming to address controversies observed in the surface contribution to the mechanical properties of silicon through pull-in voltage measurements in SiNW switches. The surface effect was analyzed through surface elasticity and surface stress with contrasting values assigned to them in the literature. NWs with high aspect ratios were fabricated and a numerical model was developed to study the electromechanical behavior of a SiNW switch. Moreover, a methodology and measurement procedure were proposed to extract the surface elasticity and surface stress parameters by utilizing the experimental and numerical results. Specifically, the following achievements were reported:

- It was observed that AR plays an important role in determining the extent of the surface stress effect. In low ARs, NWs with various thicknesses have the same $\bar{V}_{pi}$, and as the AR increases, the pull-in values for different thicknesses divert from each other. The surface effect will reduce the V_{pi} for fixed-fixed beams, whereas in cantilevers it will increase the pull-in.

- Increasing NW length with constant AR will decrease the $\bar{V}_{pi}$ for fixed-fixed NW while increasing it for the cantilever boundary condition. In both cases, the effect of changing length in a small AR is insignificant. Thus once more it is concluded that AR is a better independent parameter to model the surface effect in NWs. It has been also shown that, this size dependency appears when surface area to volume of a feature increases.

- The potential to merge the FE-SPL method in a mix and match technique for fabricating ultra-thin SiNWs was demonstrated. The SiNWs with a critical dimension of 30 nm were integrated with electrodes. A minimum gap of about 45 nm between SiNWs and electrodes is obtained. The use of FE-SPL addresses the existing challenge in available techniques on alignment of nanofeatures with a critical dimension below 50 nm.

- A method was proposed for surface characterization of SiNWs based on pull-in measurements. This method combines the numerical scheme developed in chapter 2 and the electromechanical properties of the NWs in chapter 3 to extract the surface parameters based on the algorithm in chapter 4. The numerical method is fully developed following the fabrication of Si NWs with high aspect ratios. Measurements areto be carried out in the next step. To extend this research, resonance frequency measurements will be carried out to characterize the surface parameters.

BIBLIOGRAPHY

Allain, P., Le Roux, X., Parrain, F., and Bosseboeuf, A. (2012). Large initial compressive stress in top-down fabricated silicon nanowires evidenced by static buckling. *Journal of Micromechanics and Microengineering*, 23(1):015014.

Arkan, E. F., Sacchetto, D., Yildiz, I., Leblebici, Y., and Alaca, B. E. (2011). Monolithic integration of Si nanowires with metallic electrodes: NEMS resonator and switch applications. *Journal of Micromechanics and Microengineering*, 21(12).

Aydogan, C., Hofmann, M., Rangelow, I., Bicer, M., Yalcinkaya, A., Torun, H., Volland, B., Ates, O., Lenk (geb. Hamann, C., and Alaca, B. (2018). Fabrication of optical nanodevices through field-emission scanning probe lithography and cryogenic etching. *Novel Patterning Technologies 2018*, page 51.

Babaei Gavan, K., Westra, H. J. R., Van Der Drift, E. W. J. M., Venstra, W. J., and Van Der Zant, H. S. J. (2009). Size-dependent effective Young's modulus of silicon nitride cantilevers. *Applied Physics Letters*, 94(23).

Bao, M. (2005). *Analysis and design principles of MEMS devices.* Elsevier.

Bargatin, I., Myers, E. B., Aldridge, J. S., Marcoux, C., Brianceau, P., Duraffourg, L., Colinet, E., Hentz, S., Andreucci, P., and Roukes, M. L. (2012). Large-scale integration of nanoelectromechanical systems for gas sensing applications. *Nano Letters*, 12(3):1269–1274.

Biswas, A., Bayer, I. S., Biris, A. S., Wang, T., Dervishi, E., and Faupel, F. (2012). Advances in top-down and bottom-up surface nanofabrication: Techniques, applications & future prospects. *Advances in Colloid and Interface Science*, 170(1-2):2–27.

Bolten, J., Wahlbrink, T., Schmidt, M., Gottlob, H. D., and Kurz, H. (2011). Implementation of electron beam grey scale lithography and proximity effect correction for silicon nanowire device fabrication. *Microelectronic Engineering*, 88(8):1910–1912.

Cleland, A. N. and Roukes, M. L. (1996). Fabrication of high frequency nanometer scale mechanical resonators from bulk si crystals. *Applied Physics Letters*, 69(18):2653–2655.

Ekinci, K. L. and Roukes, M. L. (2006). Nanoelectromechanical systems. *REVIEW OF SCIENTIFIC INSTRUMENTS*, 061101(2005).

Erdem Alaca, B. (2009). Integration of one-dimensional nanostructures with microsystems: an overview. *International Materials Reviews*, 54(5):245–282.

Esfahani, M. N. and Alaca, B. E. (2019). A Review on Size-Dependent Mechanical Properties of Nanowires. *Nano Letters*, 1900192:1–23.

Esfahani, M. N., Kilinc, Y., Karakan, M. Ç., Orhan, E., Hanay, M. S., Leblebici, Y., and Alaca, B. E. (2018a). Piezoresistive silicon nanowire resonators as embedded building blocks in thick soi. *Journal of Micromechanics and Microengineering*, 28(4):045006.

Esfahani, M. N., Kilinc, Y., Karakan, M. Ç., Orhan, E., Hanay, M. S., Leblebici, Y., and Alaca, B. E. (2018b). Piezoresistive silicon nanowire resonators as embedded building blocks in thick SOI. *Journal of Micromechanics and Microengineering*, 28(4):045006.

Feng, X. L., He, R., Yang, P., and Roukes, M. L. (2007). Very high frequency silicon nanowire electromechanical resonators. *Nano Letters*, 7(7):1953–1959.

Fu, Y. and Zhang, J. (2011). Size-dependent pull-in phenomena in electrically actuated nanobeams incorporating surface energies. *Applied Mathematical Modelling*, 35(2):941–951.

Garnett, E. and Yang, P. (2010). Light trapping in silicon nanowire solar cells. *Nano letters*, 10(3):1082–1087.

Goldberger, J., Hochbaum, A. I., Fan, R., and Yang, P. (2006). Silicon vertically integrated nanowire field effect transistors. *Nano letters*, 6(5):973–977.

Goosen, J. F. L., Bossche, A., French, P. J., Sadeghian, H., van der Drift, E., Yang, C. K., and van Keulen, F. (2009). Supplement, Characterizing size-dependent effective elastic modulus of silicon nanocantilevers using electrostatic pull-in instability. *Applied Physics Letters*, 94(22):221903.

Han, J. W., Ahn, J. H., Kim, M. W., Lee, J. O., Yoon, J. B., and Choi, Y. K. (2010). Nanowire mechanical switch with a built-in diode. *Small*, 6(11):1197–1200.

He, R., Feng, X. L., Roukes, M. L., and Yang, P. (2008). Monolithic self-transducing silicon nanowire electromechanical systems. *Materials Science*, pages 1–19.

He, R., Gao, D., Fan, R., Hochbaum, A. I., Carraro, C., Maboudian, R., and Yang, P. (2005). Si nanowire bridges in microtrenches: Integration of growth into device fabrication. *Advanced Materials*, 17(17):2098–2102.

Hochbaum, A. I., Fan, R., He, R., and Yang, P. (2005). Controlled growth of si nanowire arrays for device integration. *Nano letters*, 5(3):457–460.

Hu, J., Ouyang, M., Yang, P., and Lieber, C. M. (1999). Controlled growth and electrical properties of heterojunctions of carbon nanotubes and silicon nanowires. *Nature*, 399(6731):48.

Hu, S. (1998). Fabrication of silicon and metal nanowires and dots using mechanical atomic force lithography. *Journal of Vacuum Science & Technology B: Microelectronics and Nanometer Structures*, 16(5):2822.

Hu, Y. C., Chang, C. M., and Huang, S. C. (2004). Some design considerations on the electrostatically actuated microstructures. *Sensors and Actuators, A: Physical*, 112(1):155–161.

Huang, M. H., Mao, S., Feick, H., Yan, H., Wu, Y., Kind, H., Weber, E., Russo, R., and Yang, P. (2001). Room-temperature ultraviolet nanowire nanolasers. *science*, 292(5523):1897–1899.

Ionescu, A. and Riel, H. (2011). Tunnel field-effect transistors as energy-efficient electronic switches. *Nature*, 479:329–37.

Juhasz, R., Elfström, N., and Linnros, J. (2005). Controlled fabrication of silicon nanowires by electron beam lithography and electrochemical size reduction. *Nano Letters*, 5(2):275–280.

Kaestner, M., Hofer, M., and Rangelow, I. W. (2013). Mix & match electron beam & scanning probe lithography for high throughput sub-10 nm lithography. *Alternative Lithographic Technologies V*, 8680(March 2013):868019.

Kim, H., Lee, H. B. R., and Maeng, W. J. (2009). Applications of atomic layer deposition to nanofabrication and emerging nanodevices. *Thin Solid Films*, 517(8):2563–2580.

Kind, H., Yan, H., Messer, B., Law, M., and Yang, P. (2002). Nanowire ultraviolet photodetectors and optical switches. *Advanced materials*, 14(2):158–160.

Kozinsky, I., Postma, H. C., Bargatin, I., and Roukes, M. (2006a). Tuning nonlinearity, dynamic range, and frequency of nanomechanical resonators. *Applied Physics Letters*, 88(25):253101.

Kozinsky, I., Postma, H. W. C., Bargatin, I., and Roukes, M. L. (2006b). Tuning nonlinearity, dynamic range, and frequency of nanomechanical resonators. *Applied Physics Letters*, 88(25):253101.

Law, M., Goldberger, J., and Yang, P. (2004). Semiconductor nanowires and nanotubes. *Annu. Rev. Mater. Res.*, 34:83–122.

Law, M., Greene, L. E., Johnson, J. C., Saykally, R., and Yang, P. (2005). Nanowire dye-sensitized solar cells. *Nature materials*, 4(6):455.

Lenk, C., Hofmann, M., Lenk, S., Kaestner, M., Ivanov, T., Krivoshapkina, Y., Nechepurenko, D., Volland, B., Holz, M., Ahmad, A., Reum, A., Wang, C., Jones, M., Durrani, Z., and Rangelow, I. W. (2018). Nanofabrication by field-emission scanning probe lithography and cryogenic plasma etching. *Microelectronic Engineering*, 192:77–82.

Lenk, C., Krivoshapkina, Y., Hofmann, M., Lenk, S., Ivanov, T., Rangelow, I. W., Ahmad, A., Reum, A., Holz, M., Glinsner, T., Eibelhuber, M., Treiblmayr, D., Schamberger, B., Chouiki, M., Chan, B. T., el Otell, Z., and de Marneffe, J.-F. (2019). High-throughput process chain for single electron transistor devices based on field-emission scanning probe lithography and Smart Nanoimprint lithography technology. *Journal of Vacuum Science & Technology B*, 37(2):021603.

Lenk, S., Kaestner, M., and Lenk, C. (2017). 2D Simulation of Fowler-Nordheim Electron Emission in Scanning Probe Lithography. *Journal of Nanomaterials & Molecular Nanotechnology*, 06(06).

Li, D., Wu, Y., Kim, P., Shi, L., Yang, P., and Majumdar, A. (2003a). Thermal conductivity of individual silicon nanowires. *Applied Physics Letters*, 83(14):2934–2936.

Li, Q., Koo, S. M., Edelstein, M. D., Suehle, J. S., and Richter, C. A. (2007). Silicon nanowire electromechanical switches for logic device application. *Nanotechnology*, 18(31).

Li, X., Ono, T., Wang, Y., and Esashi, M. (2003b). Ultrathin single-crystalline-silicon cantilever resonators: Fabrication technology and significant specimen size effect on Young's modulus. *Applied Physics Letters*, 83(15):3081–3083.

Lieber, C. M. and Morales, A. M. (1998). A laser ablation method for the synthesis of crystalline semiconductor nanowires. *Science*, 279(5348):208–211.

Lu, W. and Lieber, C. M. (2010). Nanoelectronics from the bottom up. In *Nanoscience*

And Technology: A Collection of Reviews from Nature Journals, pages 137–146. World Scientific.

Ma, J. B., Jiang, L., and Asokanthan, S. F. (2010). Influence of surface effects on the pull-in instability of NEMS electrostatic switches. *Nanotechnology*, 21(505708).

Miller, R. E. and Shenoy, V. B. (2000). Size-dependent elastic properties of nanosized structural elements. *Nanotechnology*, 94.

Nasr, M. and Alaca, B. E. (2018). Surface Stress Effect on Silicon Nanowire Mechanical Behavior : Size and Orientation Dependence. *Mechanics of Materials*, 127(September):112–123.

Nasr Esfahani, M. and Alaca, B. E. (2019). A review on size-dependent mechanical properties of nanowires. *Advanced Engineering Materials*, page 1900192.

Ou, K. and Chen, K. (2014). Pull-in voltage estimation of microcantilever beams with effects of residual stress gradients and capacitance fringing. *IEEE Transactions on Device and Materials Reliability*, 14(1):577–579.

Rogers, J. A., Paul, K. E., Jackman, R. J., and Whitesides, G. M. (1997). Using an elastomeric phase mask for sub-100 nm photolithography in the optical near field. *Applied Physics Letters*, 70(20):2658–2660.

Sadeghian, H., Goosen, J. F. L., Bossche, A., French, P. J., van der Drift, E., Yang, C. K., and van Keulen, F. (2009). Characterizing size-dependent effective elastic modulus of silicon nanocantilevers using electrostatic pull-in instability. *Applied Physics Letters*, 94(22):221903.

Song, F., Huang, G. L., Park, H. S., and Liu, X. N. (2011). A continuum model for the mechanical behavior of nanowires including surface and surface-induced initial stresses. *International Journal of Solids and Structures*, 48(14-15).

Suntola, T. (1989). Atomic layer epitaxy. *Materials Science Reports*, 4(5):261–312.

Tasdemir, Z., Peric, O., Sacchetto, D., Fantner, G. E., Leblebici, Y., and Alaca, B. E. (2015). Monolithic fabrication of silicon nanowires bridging thick silicon structures. *IEEE Nanotechnology Express*, 1:2–5.

Wagner, R. S. and Ellis, W. C. (1964). Vapor-Liquid-Solid Mechanism of Single Crystal Growth. *Applied Physics Letters*, 4(5):89–90.

Wang, K. F. and Wang, B. L. (2014). Influence of surface energy on the non-linear pull-in instability of nano-switches. *International Journal of Non-Linear Mechanics*, 59.

Xia, Y., Yang, P., Sun, Y., Wu, Y., Mayers, B., Gates, B., Yin, Y., Kim, F., and Yan, H. (2003). One-dimensional nanostructures: synthesis, characterization, and applications. *Advanced materials*, 15(5):353–389.

Yang, Y. T., Callegari, C., Feng, X. L., Ekinci, K. L., and Roukes, M. L. (2006). Zeptogram-scale nanomechanical mass sensing. *Nano Letters*, 6(4):583–586.

Yuan, J. S. and Liou, J. J. (2013). *Semiconductor device physics and simulation*. Springer Science & Business Media.

Yun, G. and Park, H. S. (2012). Bridging the gap between experimental measurements and atomistic predictions of the elastic properties of silicon nanowires using multiscale modeling. *Finite Elements in Analysis and Design*, 49(1).

Zhang, Y., Zhuo, L. J., and Zhao, H. S. (2013). Determining the effects of surface elasticity and surface stress by measuring the shifts of resonant frequencies. *Proceedings of the Royal Society A: Mathematical, Physical and Engineering Sciences*, 469(2159).

Zoellner, J.-P., Holz, M., Reum, A., Durrani, Z., Jones, M. E., Aydogan, C., Bicer, M., Alaca, E. B., Kuehnel, M., Fröhlich, T., Manske, E., Fuessl, R., Rangelow, I. W., Kaestner, M., Lenk, C., Ahmad, A., Ivanov, T., Lenk, S., Hofmann, M., Guliyev, E., Reuter, C., and Budden, M. (2018). Field-emission scanning probe lithography with self-actuating and self-sensing cantilevers for devices with single digit nanometer dimensions. *PROCEEDINGS OF SPIE*, 1058406(March 2018):5.